IEEE Access
Multidisciplinary | Rapid Review | Open Access Journal

Received July 17, 2020, accepted August 3, 2020, date of publication August 5, 2020, date of current version August 18, 2020.

Digital Object Identifier 10.1109/ACCESS.2020.3014532

Development of a New Medical Robot System for Minimally Invasive Surgery

GUOJUN NIU[1,2], BO PAN[2], YILI FU[2], AND CUICUI QU[3]

[1]School of Mechanical Engineering and Automation, Zhejiang Sci-Tech University, Hangzhou 310018, China
[2]State Key Laboratory of Robotics and System, Harbin Institute of Technology, Harbin 150001, China
[3]Hangzhou SIASUN Robot and Automation Company Ltd., Hangzhou 311200, China

Corresponding author: Guojun Niu (niuguojun@zstu.edu.cn)

This work was supported in part by the National Natural Science Foundation of China under Grant 61803341, in part by the Natural Science Foundation of Zhejiang Province under Grant LY20E050019, and in part by the State Key Laboratory of Robotics and System (HIT) under Grant SKLRS-2019-KF-08.

ABSTRACT This article presents the development of a new medical robot system comprising a spherical remote center motion (RCM) mechanism with modular design and two mechanical decoupling methods for Minimally Invasive Surgery (MIS). We achieved excellent comprehensive performance indices through a novel multi-objective optimization model comprising four optimization objective functions, three constrained conditions and two optimization variables. In order to enhance the manipulability, remove the coupling between motors, and reduce the control difficulty, two new decoupling mechanism means were proposed to remove coupling motion between the wrist and pincers, coupling motion between the translational joint of mobile platform and four interface disks of surgical instrument as a results of rear drive motor, respectively. The control system architecture is designed to include intuitive motion control, incremental motion control, and proportional motion control. Master-slave attitude registration and surgical instrument replacement strategies improve the master-slave control efficiency. We tested the spherical RCM mechanism performance indices and developed two mechanical decoupling methods and a master–slave control algorithm. Our experimental test results validated that fixing point accuracy, the coupling motions, the positioning and repeated positioning accuracy of the MIS robot, and master–slave control algorithm meet the requirements of MIS. Successful animal experiments confirmed effectiveness of the novel MIS robot system.

INDEX TERMS MIS robot, multi-objective optimization, decoupling motion, master-slave control, RCM.

I. INTRODUCTION

Minimally invasive surgery (MIS) has developed rapidly and become increasingly popular. The advantages of MIS include less trauma, fewer postoperative diseases, and faster recovery. Traditional MIS is usually done by inserting a surgical instrument (SI) into the patient through a small incision. However, this method has some disadvantages including poor flexibility, easy fatigue, impaired depth perception, and limited surgical field of vision. MIS robot technology holds the key to solving these difficulties. Motion around a pivot point with two rotational degrees of freedom (DOF) and one translational DOF is achieved by mechanical constraints. There are three types of remote center motion (RCM) mechanisms: parallel [1]–[3], serial-parallel [4] and serial. This article mainly focuses on serial RCM mechanisms. There are four kinds of mechanisms achieving motion constraints around a fixed point: passive joint mechanisms, parallelogram mechanisms, circular guide mechanisms, and spherical mechanisms. Some advantages and disadvantages of four methods are explained below.

(1) Multi-joint and linkage passive joint mechanisms are used in many MIS robots [5]–[7]. One advantage of this mechanism is that the trocar can be rotated freely according to the pivot point. It has greater robustness and better safety should the trocar position change due to the patient's accidental movement. The disadvantage of this mechanism is that its operational accuracy is often disturbed by the elastic characteristics of the abdomen [8].

(2) Parallelogram mechanisms are widely used to implement RCM in many MIS robots [9]–[14]. There are two methods applied in surgical robot design: the multi-parallelogram

The associate editor coordinating the review of this manuscript and approving it for publication was Hamid Mohammad-Sedighi.

mechanism and the open-loop parallelogram with synchronous belt constraints. Although it has high rigidity, the multi-parallelogram mechanism is cumbersome as a result of the many joints and links involved and requires high processing accuracy to prevent deadlock [8]. The open-loop parallelogram with time belt constraints has only three joints and links, but the assembly is more complex, the mechanism stiffness is reduced, and maintenance and repair costs are increased.

(3) The circular guidance mechanism used to implement RCM in MIS robot design [15]–[17] is relatively simple, but its stainless steel circular track is three times heavier than the aluminum link and its volume is relatively large [8].

(4) The spherical mechanism with two rotational joints used for RCM MIS robot design [8], [18]–[22] has two configurations: series and parallel. Because the links of parallel spherical mechanism readily collide with each other [18], serial configuration is most commonly used. The wire drive used in serial spherical RCM design has shortcomings including low rigidity, poor safety, inability to achieve modular design, and increased maintenance and repair costs. Hence, the development of a spherical RCM mechanism with modular design would be preferable.

Parallel wrist [23], snake-like [24], [25], and wire-driven wrist [26] devices may improve the dexterity of SIs. However, taking dexterity, sterilization, volume, mass, and cost of SI into account, the wire-driven wrist is the most efficient and extensively used by intuitive surgical robots. However, it results in a coupling motion between wrist and forceps that is problematic [27], [28]. Algorithm and mechanical compensation methods can be used to overcome this problem.

The algorithm method avoids the complex mechanical coupling design. Several types of SIs are used in surgery and SI replacement often occurs. When one type of SI is replaced with another, the new SI must be identified by system, and the corresponding compensating algorithms registered, which increases SI exchange times. With the popularization and broader application of MIS robots in surgery, new SIs will be designed, and the corresponding compensating algorithms updated in all MIS robot systems. This impacts negatively on the universality of software control algorithms. For these two reasons, the mechanical decoupling design is used to eliminate the coupling motion.

In order to reduce exchange times, improve the universality of software control algorithms, remove the coupling between motors, reduce costs, and promote the application of MIS robots, it is necessary to improve and enhance SIs and eliminate coupling motion.

The article is organized as follows: Section II presents kinematic analysis of the RCM mechanism. Section III solves the optimization of the RCM mechanism to obtain excellent comprehensive performance indices. Section IV introduces the concept design of the novel MIS robot. The master–slave control design is provided in Section V. The auxiliary control strategy presented in Section VI consists of the master–slave posture registration and SI replacement strategy. Section VII describes the experimental testing of the two mechanical decoupling methods, the positioning accuracy and repeated positioning accuracy of the MIS robot, and verification of the master–slave control algorithm, and cholecystectomy and nephrectomy in pigs to validate the effectiveness of the corresponding designs. Section VIII concludes the article.

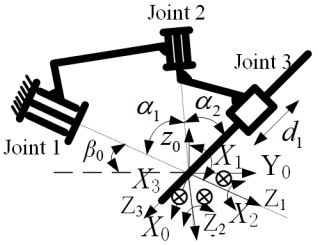

FIGURE 1. The D-H coordinate of the spherical RCM mechanism.

TABLE 1. D-H parameters of the spherical RCM mechanism.

i	α_{i-1}/rad	a_i/mm	d_i/mm	θ_i/rad
1	α_0	0	0	θ_1
2	α_1	0	0	θ_2
3	α_2	0	d	0

II. KINEMATIC ANALYSIS OF RCM MECHANISM

A. FORWARD AND INVERSE KINEMATICS

D-H coordinate system of spherical RCM mechanism is demonstrated in Figure 1. The D-H parameters of the spherical RCM mechanism are listed in Table 1, homogeneous transfer matrixes are calculated and forward kinematics can be obtained, then, the position vector (p_x, p_y, p_z) of wrist is expressed by (1), as shown at the bottom of the page. Based on (1), The inverse kinematics (q_1, q_2, q_3) of wrist position is given by (2).

$$\begin{aligned}
d_3 &= \sqrt{(p_x)^2 + (p_y)^2 + (p_z)^2}, \\
\theta_2 &= \arctan 2\left(\pm\sqrt{1-k^2},\ k\right), \\
\theta_1 &= \arctan 2\left(k_2,\ k_1\right), \\
k &= (p_y s\alpha_0 - p_z c\alpha_0 + d_3 c\alpha_1 c\alpha_2)/(d_3 s\alpha_1 s\alpha_2), \\
k_1 &= p_x s\alpha_2 s_2 - (p_y c\alpha_0 + p_z s\alpha_0)(c\alpha_1 s\alpha_2 c_2 + s\alpha_1 c\alpha_2), \\
k_2 &= p_x(c\alpha_1 s\alpha_2 c_2 + s\alpha_1 c\alpha_2) + s\alpha_2 s_2(p_y c\alpha_0 + p_z s\alpha_0)
\end{aligned} \quad (2)$$

where $c_1 = \cos(\theta_1)$, $s_1 = \sin(\theta_1)$, $c_2 = \cos(\theta_2)$, $s_2 = \sin(\theta_2)$, $c\alpha_0 = \cos(\alpha_0)$, $s\alpha_0 = \sin(\alpha_0)$, $c\alpha_1 = \cos(\alpha_1)$, $s\alpha_1 = \sin(\alpha_1)$, $c\alpha_2 = \cos(\alpha_2)$, $s\alpha_2 = \sin(\alpha_2)$, $\alpha_0 = -(\beta_0 + 0.5\pi)$.

$$\begin{bmatrix} p_x \\ p_y \\ p_z \end{bmatrix} = \begin{bmatrix} d_3 s\alpha_2 c_1 s_2 + d_3 c\alpha_1 s\alpha_2 s_1 c_2 + d_3 s\alpha_1 c\alpha_2 s_1 \\ d_3 c\alpha_0 s\alpha_2 s_1 s_2 - d_3 c\alpha_0 c\alpha_1 s\alpha_2 c_1 c_2 - d_3 c\alpha_0 s\alpha_1 c\alpha_2 c_1 + d_3 s\alpha_0 s\alpha_1 s\alpha_2 c_2 - d_3 s\alpha_0 c\alpha_1 c\alpha_2 \\ d_3 s\alpha_0 s\alpha_2 s_1 s_2 - d_3 s\alpha_0 c\alpha_1 s\alpha_2 c_1 c_2 - d_3 s\alpha_0 s\alpha_1 c\alpha_2 c_1 - d_3 c\alpha_0 s\alpha_1 s\alpha_2 c_2 + d_3 c\alpha_0 c\alpha_1 c\alpha_2 \end{bmatrix} \quad (1)$$

B. JACOBIAN MATRIX

The Jacobian matrix has a wide range of applications in mechanism optimization, the Jacobian of the spherical RCM mechanism with two rational DOFs is expressed by (3).

$$\boldsymbol{J} = \begin{bmatrix} s\alpha_1 s_2 & 0 \\ s\alpha_1 c_2 c\alpha_2 + c\alpha_1 s\alpha_2 & s\alpha_2 \end{bmatrix} \tag{3}$$

III. OTPIMIZATION OF RCM MECHANISM

Some optimizations of the spherical RCM mechanism performance have been achieved. Nouaille presented an optimal choice of geometrical parameters of a global function in relation to kinematic performance and compactness indices [29]. An optimization model consisting of workspace size, the new manipulability index and mechanism size for spherical RCM mechanisms was proposed by Zhang and Nelson [30]. Lum put forward a synthesis model including the kinematic index and stiffness to optimize the spherical RCM mechanism [18]. In the current article, a comprehensive multi-objective model with four optimization objective functions (an improvement global kinematic index, a compactness index, a global comprehensive stiffness index, and global dynamic index), three constrained conditions (workspace constraint, mechanical parameter constraint, and mass constraint) and two optimization variables (α_1 and α_2) is constructed to optimize the spherical RCM mechanism using the NSGA-II algorithm.

A. OPTIMIZATION OBJECTIVES

1) KINEMATIC PERFORMANCE INDEX

The global performance index (GPI) for kinematic optimization [31] is expressed by (4).

$$\eta = \int_w k \mathrm{d}w \Big/ \int_w \mathrm{d}w \tag{4}$$

where k is velocity isotropy [32], w is workspace.

The improvement of the GPI for dimensional homogenization is expressed by (5).

$$f_1 = 1 - \frac{\eta}{\max(\eta)} \tag{5}$$

2) COMPACTNESS INDEX

The parameters α_1 and α_2 determine the volume of the spherical mechanism. $\alpha_{1\max} = \alpha_{2\max} = 0.5\pi$. Compactness index is defined by (6).

$$f_2 = \frac{\alpha_1 + \alpha_2}{\pi} \tag{6}$$

3) STIFFNESS INDEX

The condition number of the translation and rotation stiffness matrix [33] is expressed by (7) to indicate stiffness variation of the mechanism.

$$k_\mathrm{t} = \|\boldsymbol{K}_\mathrm{t}\| \left\|\boldsymbol{K}_\mathrm{t}^{-1}\right\| \quad k_\mathrm{r} = \|\boldsymbol{K}_\mathrm{r}\| \left\|\boldsymbol{K}_\mathrm{r}^{-1}\right\| \tag{7}$$

where $\|\boldsymbol{K}_\mathrm{i}\| = \sqrt{\mathrm{tr}(\boldsymbol{K}_\mathrm{i}\boldsymbol{\omega}\boldsymbol{K}_\mathrm{i}^\mathrm{T})}$, i represents t and r, t and r denotes translation and rotation, respectively, [34].

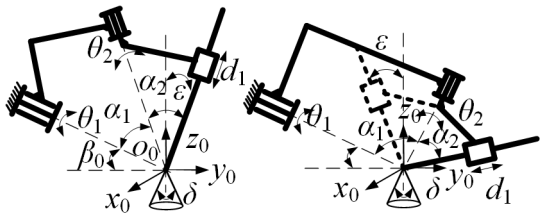

FIGURE 2. Workspace when $\alpha_1 + \alpha_2 + \beta_0 \le \pi$ and $0 \le \beta_0 \le 0.25\pi$: (a) $\alpha_1 + \beta_0 \le 0.5\pi$; (b) $\alpha_1 + \beta_0 \ge 0.5\pi$.

The GPI of condition number is defined by (8). Improvement of the GPI is expressed by (9). The comprehensive stiffness performance index is expressed by (10).

$$\varsigma_i = \int_w k_i \mathrm{d}w \Big/ \int_w \mathrm{d}w \tag{8}$$

$$S_i = 1 - \varsigma_i / Max(\varsigma_i) \tag{9}$$

$$f_3 = (S_\mathrm{t} + S_\mathrm{r})/2 \tag{10}$$

where i represents t and r, respectively.

4) DYNAMIC INDEX

In surgery, taking low velocity and external forces into consideration. The dynamic model [35] of RCM mechanism can be simplified as follows.

$$\boldsymbol{\tau} = \boldsymbol{M}(q)\ddot{q} + \boldsymbol{G}(q) \tag{11}$$

The GPI [36] of dynamics is expressed by (12). The improvement of GPI of dynamics is given by (13).

$$\gamma_\tau = \sum_{i=1}^{n} \frac{\int |\boldsymbol{\tau}_i \boldsymbol{\omega}_i| \, \mathrm{d}w}{w} \tag{12}$$

where n is number of joints, $\boldsymbol{\omega}$ is angular velocity of joint, w is workspace of robot.

$$f_4 = \frac{\gamma_\tau}{Max(\gamma_\tau)} \tag{13}$$

B. CONSTRAINTS

1) WORKSPACE CONSTRAINT

A cone with vertex angle 90° is required in surgery [18]. The δ shown in Figure 2 is calculated by (14). The workspace constraint is expressed by (14).

$$\delta = \begin{cases} 2\varepsilon = 2\left(\alpha_1 + \alpha_2 + \beta_0 - 0.5\pi\right) & \text{if } \alpha_1 + \beta_0 \le 0.5\pi \\ 2\varepsilon = 2\left(\alpha_2 - (\alpha_1 + \beta_0 - 0.5\pi)\right) & \text{if } \alpha_1 + \beta_0 \ge 0.5\pi \\ \text{and } \alpha_2 \ge (\alpha_1 + \beta_0 - 0.5\pi) & \\ 0 \quad \text{if } \alpha_1 + \beta_0 \ge 0.5\pi \text{ and } \alpha_2 \le \alpha_1 + \beta_0 - 0.5\pi & \end{cases} \tag{14}$$

$$\delta \ge 0.5\pi \tag{15}$$

2) MECHANICAL PARAMETER CONSTRAINT

Taking two rational DOFs of the RCM mechanism into consideration, the workspace area of the ellipsoid surface is expressed by (16) as shown in Figure 3 (a). The area S_W is symmetric with the plane $\alpha_1 = \alpha_2$. However, GPI shown in Figure 3 (b) is asymmetric with the plane $\alpha_1 = \alpha_2$. The value of η when $\alpha_1 \geq \alpha_2$ is larger than the value of η when $\alpha_1 < \alpha_2$. The mechanical parameter constraint is expressed by (17).

$$\begin{aligned} S_W &= \iint_{\Sigma} ds \\ &= \iint_{\Sigma} \sqrt{\left(\frac{\partial(y,z)}{\partial(q_1,q_2)}\right)^2 + \left(\frac{\partial(x,z)}{\partial(q_1,q_2)}\right)^2 + \left(\frac{\partial(x,y)}{\partial(q_1,q_2)}\right)^2} \\ &\quad \times \mathrm{d}q_1 \mathrm{d}q_2 \end{aligned} \tag{16}$$

$$\alpha_1 \geq \alpha_2 \tag{17}$$

3) MASS CONSTRAINT

The spherical RCM mechanism shown in Figure 1 contains two linkages (m_1 and m_2). The mass constraint is expressed by (18).

$$m_1 + m_2 \leq m \tag{18}$$

C. OPTIMIZATION MODEL

The dimensional optimization model comprises design variables, optimization objective functions, and constraint conditions.

Design variables: $\alpha_1 \in [0.25\pi\ 0.5\pi]$, $\alpha_2 \in [0.25\pi\ 0.5\pi]$.

Optimization objectives:

$$\min \begin{cases} f_1 = 1 - \eta / \max(\eta) \\ f_2 = (\alpha_1 + \alpha_2)/\pi \\ f_3 = (S_t + S_r)/2 \\ f_4 = \gamma_\tau / Max(\gamma_\tau) \end{cases} \tag{19}$$

Constraints:

$$g_1 : \delta \geq 0.5\pi; \quad g_2 : \alpha_1 \geq \alpha_2; \ g_3 : m_1 + m_2 \leq 3 \tag{20}$$

D. PROBLEM SOLVING

Dimensional optimization comprising four objectives is a multi-objective optimization problem. The NSGA-II algorithm [37] offers computational efficiency and global convergence and is widely used in multi-objective optimization to optimize the angles of the spherical RCM mechanism. The parameters for NSGA-II are shown in Table 2.

TABLE 2. Parameters used for the NSGA-II.

Population size	200
Maximal generation number	100
Number of design variables	2
Number of objectives	4
Number of constraints	3

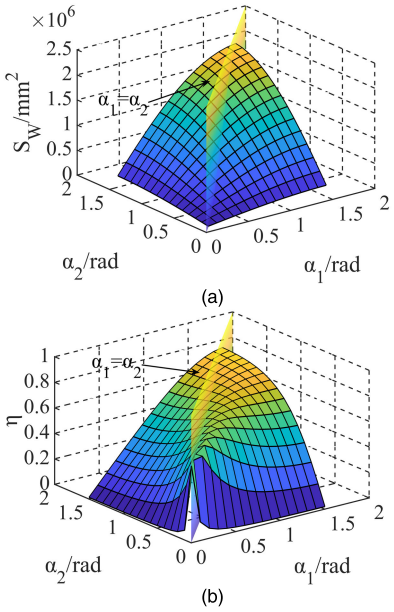

FIGURE 3. (a) The relationship between S_W and α_1, α_2; (b) The relationship between η and α_1, α_2.

The multi-objective optimization process is given as follows: (1) Derive some appropriate optimization objectives to describe the mechanism performance indices. (2) Identify design parameters and give constraints involving mechanism. (3) Initialize NSGA-II settings. (4) Combine the objectives using Pareto approach. (5) Perform multiple optimizations using different weighting or emphasis.

Variation tendencies and interdependence among α_1, α_2, f_1, f_2, f_3, and f_4 using a scatter matrix [38] are shown in Figure 4. The lower and upper triangles of the matrix show scatter plots and their corresponding correlation coefficients (R), respectively. The matrix diagonal elements present the probability density diagram of α_1, α_2, f_1, f_2, f_3, and f_4. R $\in$ [−1, 1]. R closer to −1 or 1 implies a stronger correlation between two elements. R closer to 0 indicates a weaker correlation between two elements. P value reflects the probability of an event. R is significantly different from zero when P < 0.05, indicating that the correlation between two elements is very significant.

From Figure 4:

- The correlation between every two elements of f_1, f_2, and f_4 are significant as R (−0.98) between f_1 and f_2, R (−0.71) between f_1 and f_4, R (0.84) between f_2 and f_4 are closer to −1, −1, and 1, respectively.
- The independent of f_3 with α_1, f_1, f_2 is relatively high as R (−0.21) between f_3 and α_1, R (0.25) between f_3 and f_1, R (-0.43) between f_3 and f_2 are closer to 0.
- α_2 is a strongly and positively correlated with f_2 and f_4(the two corresponding Rs (0.91, 0.92) are closer to 1), whereas it is a strongly and negatively correlated with f_1 (the corresponding R (−0.81) is closer to −1,).
- α_1 is a strongly and positively correlated with f_2(the corresponding R (0.95) is closer to 1) whereas it has strongly

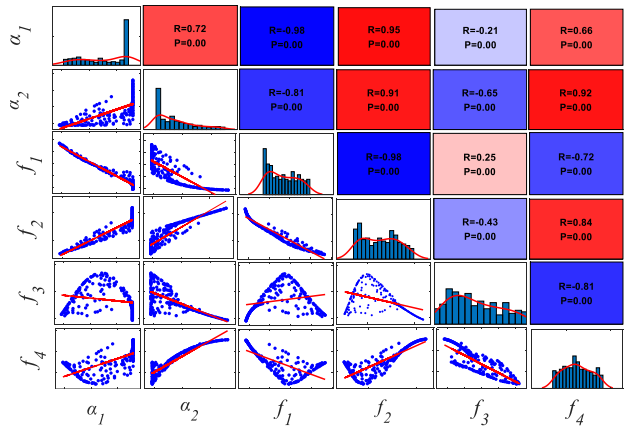

FIGURE 4. Scatter matrix.

and inversely correlated with f_1 (the corresponding R (−0.98) is closer to −1).

The above analysis shows that the correlation between f_2 and α_1, α_2 is stronger than the corresponding part between f_1, f_3, f_4 and α_1, α_2, the correlation (−0.98, −0.43, 0.84) between f_2 and f_1, f_3, f_4 is stronger than the corresponding part (−0.98, 0.25, −0.72) between f_1 and f_2, f_3, f_4, at the same time, the correlation (−0.98, −0.43, 0.84) between f_2 and f_1, f_3, f_4 is stronger than the corresponding part (0.25, −0.43, −0.81) between f_3 and f_1, f_2, f_4. In addition, high kinematic dexterity f_1, better stiffness f_3 and excellent dynamic f_4 are the optimum goal. Pareto solutions between f_2 and f_1, f_3, f_4 is shown in Figure 5.

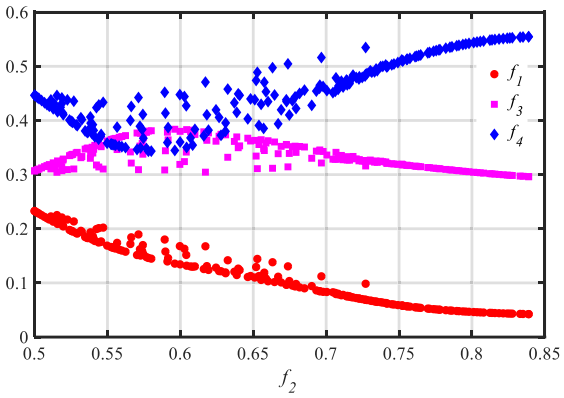

FIGURE 5. Pareto solutions between f_2 and f_1, f_3, f_4.

Ten Pareto optimal solutions obtained from the generalized feasible solutions shown in Figure 5, compared and chosen according to actual need, were selected for further consideration (Table 3). The GPI of the kinematic performance index should be high in order to successfully complete complex surgical operations requiring dexterity. Hence, improvement of the kinematic GPI was chosen as the key index. The improvement of GPI was smaller in the first, second, third, fourth, and fifth groups than in the sixth, seventh, eighth, ninth, and tenth groups. So, the last five groups were removed. In order

TABLE 3. Design variables, objective functions, and selective function.

ID	Design variables		Objective functions				Selection
	α_1 (rad)	α_2 (rad)	f_1	f_2	f_3	f_4	F_1
1	1.32	1.32	0.04	0.84	0.3	0.55	1.73
2	1.32	1.18	0.05	0.79	0.31	0.54	1.69
3	1.32	0.95	0.07	0.72	0.33	0.48	1.6
4	1.30	0.9	0.08	0.7	0.33	0.45	1.56
5	1.24	0.88	0.1	0.67	0.36	0.44	1.57
6	1.03	0.79	0.15	0.58	0.38	0.34	/
7	0.94	0.79	0.17	0.55	0.36	0.36	/
8	0.94	0.91	0.18	0.59	0.31	0.45	/
9	0.87	0.85	0.2	0.54	0.31	0.43	/
10	0.79	0.79	0.23	0.5	0.31	0.45	/

to obtain a better comprehensive solution from the remaining candidate list, a comprehensive performance index [38] $F_1 = f_1 + f_2 + f_3 + f_4$ was used as a selection index. The minimum of F1 was the fourth group, where $\alpha 1 = 1.3$ and $\alpha 2 = 0.9$ were obtained.

TABLE 4. Comparison between results of reference [39], [30] and [8].

ID	Design variables		Objective functions				Selection
	α_1 (rad)	α_2 (rad)	f_1	f_2	f_3	f_4	F_1
1	1.30	0.9	0.08	0.7	0.33	0.45	1.56
2	1.25	1.05	0.07	0.73	0.33	0.51	1.65
3	0.75	0.72	0.25	0.49	0.29	0.46	1.50
4	1.57	1.05	0.03	0.83	0.21	0.73	1.81

Similar to the findings reported by reference [39], we found that spherical RCM mechanism optimization can be achieved by nonlinear programing algorithms, however, in the previous study the scoring function was a synthesis of three individual elements and the constraint conditions were not used. Table 4 shows a comparison of the previous study results (ID 2) with the above optimization result (ID 1). The kinematic performance index is better in ID 2, however, the comprehensive performance index (F_1) is worse than that of ID 1. Reference [30] applied a genetic algorithm in spherical RCM mechanism optimization, but the constraint conditions were not used. The result, ID 3 in Table 4, showed worse kinematic performance than the ID 1. Since the kinematic performance index is crucial in order to successfully complete complex surgical operations requiring dexterity, and the improvement of kinematic GPI (f_1) is less than 0.1 in ID 3, this result does not meet the requirements. Reference [8] reported optimization of the spherical RCM mechanism using the Culling algorithm with only one objective and two constraints. The result, ID 4 in Table 4, indicated that f_1 was less than 0.1 and the comprehensive performance index (F_1) was worse than the ID1.

IV. CONCEPT DESIGN OF THE NOVEL MIS ROBOT

A. MODULAR DESIGN

Modular design has been extensively applied in industrial products because of its many advantages including low design and manufacturing costs and convenient maintenance and

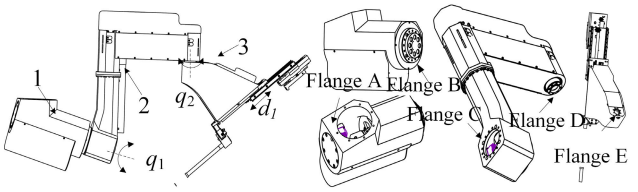

FIGURE 6. The spherical RCM mechanism prototype.

subsequent repairs. The introduction of modular design into the design process of medical robots facilitates disassembly, assembly, maintenance, and disinfection of medical robots, and hence reduces medical robot costs and expands their application in MIS. The spherical RCM mechanism model is shown in Figure 6. The spherical RCM mechanism comprises three joints. Each joint is a separate module that is easy to assemble, disassemble, and maintain.

B. DECOUPLING MECHANISM DESIGN

1) DECOUPLING DESIGN BETWEEN WRIST AND FORCEPS OF SI

Commercial SIs are designed with flexible operation in mind, however, the coupling motion between wrist and forceps in commercial SIs reduces the dexterity of the SI causing discomfort to the surgeon. The envelope angle σ_1 of the wire cable before rotation is shown in Figure 7 (a). The envelope angle σ_2 of the wire cable after rotation is shown in Figure 7 (b). The change in length of CE is expressed by (21). Δ AB is applied to compensate for ΔCE. The change in forceps rotation angle caused by the coupling motion is expressed by (22). We propose a new decoupling method to solve this problem as shown in Figure 7 (c), (d). ΔCE' is equal to zero as the wrist movement range is [$-90°$, $90°$], and the coupling motion between wrist and forceps is eliminated.

$$\Delta l = 0.5(\sigma_2 - \sigma_1)D_\theta \tag{21}$$

$$\Delta\gamma = {}^{2\Delta l}/_{D_\gamma} \tag{22}$$

where D_θ and D_γ are the diameters of wrist and pincers, respectively.

2) DECOUPLING DESIGN BETWEEN FOUR INTERFACE DISKS AND MOBILE PLATFORM

The four drive motors for the SI and one drive motor for the mobile platform are located on the link near joint 2. To reduce the drive torque of the joint 2 motor and the volume occupied by the mobile platform shown in Figure 8, the drive torque is transmitted from motors to interface disks by wire cables. However, when the mobile platform moves, the distance between the motors and the interface disks changes, and coupling motion occurs between the four interface disk rotations and the mobile platform translation. Algorithm and mechanical compensations may be used to eliminate the coupling motion. Because the maximum range of the mobile platform is 310 mm, the wire wheel

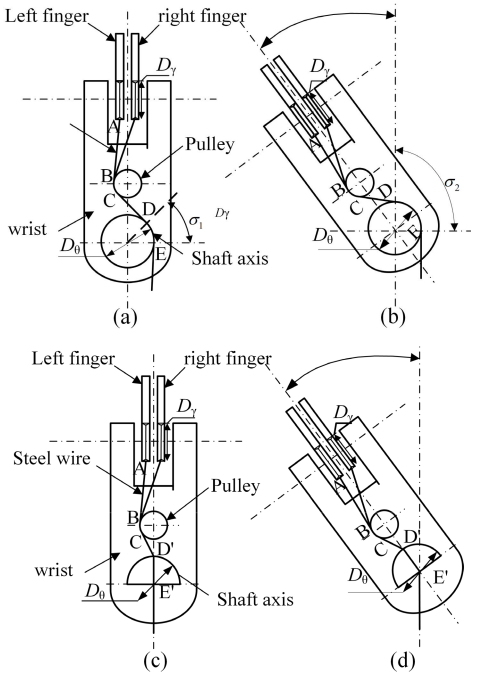

FIGURE 7. The coupling and decoupling principle between wrist and forcep. (a) The initial state of the commercial SI wrist; (b) The state of the commercial SI wrist after rotation; (c) The initial state of the improved commercial SI wrist; (d) The state of the improved commercial SI wrist after rotation.

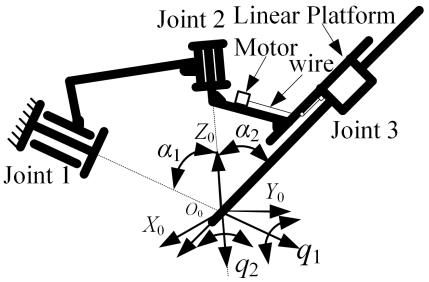

FIGURE 8. The coupling motion principle between four interface disks and mobile platform.

used to compensate for the mobile platform is very big. This leads to the larger volume of the RCM mechanism, hence the algorithm method is not a good choice and the mechanical method is therefore applied to eliminate coupling motion.

The mobile platform is divided into three sections (section 1, section 2, and section 3) as shown in Figure 9. The four interface disks (S_1, S_2, S_3, and S_4), shown in Figure 21, are mounted on section 1. The four drive motors for the SI and one drive motor for mobile platform are installed on section 3. The pulley and linear guide are fixed on section 2. Section 1 can move up and down on section 2. Section 2 can move up and down on section 3.

The wire cable routing for driving interface disks S_1 and S_2 is shown in Figure 9 (a). When the downward velocity of section 1 relative to section 2 is equal to the downward velocity of section 2 relative to section 3, shortening in the *ab* length equals the increase in the *bc* length, as the entire wire

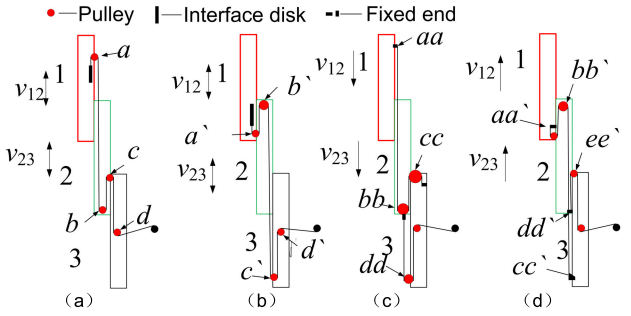

FIGURE 9. The decoupling principle of mechanism: (a) is the wire rope routing for driving interface disks S_1 and S_2; (b) is the wire rope routing for driving interface disks S_3 and S_4; (c) is the wire rope routing for achieving downward velocity $v_{12} = v_{23}$; (d) is the wire rope routing for achieving upward velocity $v_{12} = v_{23}$.

cable *ac* length does not change. When the upward velocity of section 1 relative to section 2 is equal to the upward velocity of section 2 relative to section 3, the increase in length *ab* equals the shortening in length *bc* as the entire wire cable *ac* length does not change. The decoupling design for interface disks S_1 and S_2 is thus achieved.

The wire cable routing for driving interface disks S_3 and S_4 is shown in Figure 9 (b). When the upward velocity of section 1 relative to section 2 is equal to the upward velocity of section 2 relative to section 3, shortening of the $a'b'$ length equals the increase in $b'c'$ length as the entire wire cable $a'c'$ length does not change. When the downward velocity of section 1 relative to section 2 is equal to the downward velocity of section 2 relative to section 3, the increase in the $a'b'$ length equals the shortening of the $b'c'$ length as the entire wire cable $a'c'$ length does not change. The decoupling design for interface disk S_3 and S_4 is thus achieved.

The method used to ensure that the downward velocity of section 1 relative to section 2 equals the downward velocity of section 2 relative to section 3 is shown in Figure 9 (c). According to the moving pulley theory, equation (23) is derived since $\Delta l_{bbcc} = \Delta l_{bbdd}$, and hence equation (24) is obtained.

Figure 9 (d) provides a schematic representation of how the upward velocity of section 1 relative to section 2 was made to equal the upward velocity of section 2 relative to section 3. According to the moving pulley theory, equation (25) is derived, because $\Delta l_{bb'cc'} = \Delta l_{dd'ee'}$, and hence equation (26) is obtained.

$$\Delta l_{aabb} + \Delta l_{bbcc} = 2\Delta l_{bbdd} \tag{23}$$

$$\Delta l_{aabb} = \Delta l_{bbcc} \Rightarrow \Delta l_{aabb}/\Delta t = \Delta l_{bbcc}/\Delta t \Rightarrow v_{12} = v_{23} \tag{24}$$

$$\Delta l_{aa'bb'} + \Delta l_{bb'cc'} = 2\Delta l_{dd'ee'} \tag{25}$$

$$\Delta l_{aa'bb'} = \Delta l_{bb'cc'} \Rightarrow \Delta l_{aa'bb'}/\Delta t = \Delta l_{bb'cc'}/\Delta t \Rightarrow v_{12} = v_{23} \tag{26}$$

where Δl_{aabb}, Δl_{bbcc}, Δl_{bbdd}, $\Delta l_{aa'bb'}$, $\Delta l_{bb'cc'}$ and $\Delta l_{dd'ee'}$ are the length variations of the wire *aabb*, *bbcc*, *bbdd*, *aa'bb'*, *bb'cc'* and *dd'ee'* in the period of Δt respcetively.

V. MASTER-SLAVE CONTROL DESIGN

A. FORWARD KINEMATICS OF THE SLAVE ARM

The arm holding the SI comprises nine DOFs (q_1, q_2, q_3, q_4, q_5, q_6, q_7, q_8,q_9). The arm holding endoscope consists of six DOFs (q_1, q_2, q_3, q_4, q_5, q_6). The naming convention and the zero configuration (NCZC) of the slave arm is shown in Figure 10.

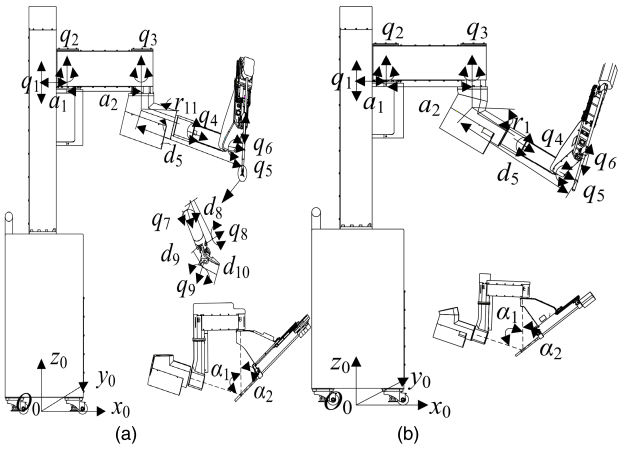

FIGURE 10. The NCZC of arm, (a) is the arm fixing SI, (b) is the arm fixing endoscopy.

To build the twists for the rotational and translational joints for the arm holding the SI, note that

$$\begin{aligned}
&\boldsymbol{\omega}_1 = \boldsymbol{\omega}_2 = \boldsymbol{\omega}_3 = \begin{bmatrix} 0 & 0 & 1 \end{bmatrix}^{\mathrm{T}}, \quad \boldsymbol{\omega}_4 = \begin{bmatrix} c_1 & 0 & -s_1 \end{bmatrix}^{\mathrm{T}}, \\
&\boldsymbol{\omega}_6 = \begin{bmatrix} -s_1 s_3 + c_1 c_2 c_3 & -s_2 c_3 & -s_1 c_2 c_3 - c_1 s_3 \end{bmatrix}^{\mathrm{T}}, \\
&\boldsymbol{\omega}_7 = \begin{bmatrix} -s_1 s_3 + c_1 c_2 c_3 & -s_2 c_3 & -s_1 c_2 c_3 - c_1 s_3 \end{bmatrix}^{\mathrm{T}}, \\
&\boldsymbol{\omega}_8 = \begin{bmatrix} -s_1 c_3 - c_1 c_2 s_3 & s_2 s_3 & s_1 c_2 s_3 - c_1 c_3 \end{bmatrix}^{\mathrm{T}}, \\
&\boldsymbol{\omega}_5 = \begin{bmatrix} c_1 c_2 & -s_2 & -c_2 s_1 \end{bmatrix}^{\mathrm{T}}, \quad \boldsymbol{\omega}_9 = \begin{bmatrix} -c_1 s_2 & c_2 & -s_1 s_2 \end{bmatrix}^{\mathrm{T}}
\end{aligned} \tag{27}$$

where $s_1 = \sin(r_{11})$, $c_1 = \cos(r_{11})$, $s_2 = \sin(\alpha_1)$, $c_2 = \cos(\alpha_1)$, $s_3 = \sin(\alpha_2)$, $c_3 = \cos(\alpha_2)$.

To build the twists for the rotational and translational joints for the arm holding endoscope, note that

$$\begin{aligned}
&\boldsymbol{\omega}_1 = \boldsymbol{\omega}_2 = \boldsymbol{\omega}_3 = \begin{bmatrix} 0 & 0 & 1 \end{bmatrix}^{\mathrm{T}}, \\
&\boldsymbol{\omega}_5 = \begin{bmatrix} c_{11} c_2 & -s_2 & -c_2 s_{11} \end{bmatrix}^{\mathrm{T}} \\
&\boldsymbol{\omega}_4 = \begin{bmatrix} c_{11} & 0 & -s_{11} \end{bmatrix}^{\mathrm{T}}, \\
&\boldsymbol{\omega}_6 = \begin{bmatrix} -s_{11} s_3 + c_{11} c_2 c_3 & -s_2 c_3 & -s_{11} c_2 c_3 - c_{11} s_3 \end{bmatrix}^{\mathrm{T}}
\end{aligned} \tag{28}$$

and the axis points for the arm holding SI are selected as (29), shown at the bottom of the next page, and the axis points for the arm folding endoscope are selected as

$$\begin{aligned}
&\boldsymbol{p}_1 = \begin{bmatrix} 0 & 0 & 0 \end{bmatrix}^{\mathrm{T}}, \ \boldsymbol{p}_2 = \begin{bmatrix} 0 & a_1 & d_1 \end{bmatrix}^{\mathrm{T}}, \\
&\boldsymbol{p}_3 = \begin{bmatrix} 0 & a_1 + a_2 & d_1 \end{bmatrix}^{\mathrm{T}}, \\
&\boldsymbol{p}_4 = \boldsymbol{p}_5 = \boldsymbol{p}_6 = \begin{bmatrix} a_1 + a_2 + d_5 c_{11} & 0 & d_1 - d_5 s_{11} \end{bmatrix}^{\mathrm{T}}
\end{aligned} \tag{30}$$

This yields twists for a rotational joint

$$\boldsymbol{\xi}_i = \begin{bmatrix} \boldsymbol{\omega}_i & \boldsymbol{p}_i \times \boldsymbol{\omega}_i \end{bmatrix}^T, \quad i = 1, 2, 3, \cdots, 8, 9 \tag{31}$$

This yields twists for a translational joint

$$\boldsymbol{\xi}_i = \begin{bmatrix} 0 & \boldsymbol{v_i} \end{bmatrix}^T, \quad i = 1, 2, 3, \cdots, 8, 9 \tag{32}$$

and the zero configuration of the arms holding the SI and endoscope are expressed by (33) and (34), as shown at the bottom of the page, respectively.

The forward kinematics of the arm holding the SI and endoscope are expressed by (35) and (36), respectively.

$$\boldsymbol{g}_{st}(q) = e^{\hat{\boldsymbol{\xi}}_1 q_1} e^{\hat{\boldsymbol{\xi}}_2 q_2} e^{\hat{\boldsymbol{\xi}}_3 q_3} e^{\hat{\boldsymbol{\xi}}_4 q_4} e^{\hat{\boldsymbol{\xi}}_5 q_5} e^{\hat{\boldsymbol{\xi}}_6 q_6} e^{\hat{\boldsymbol{\xi}}_7 q_7} e^{\hat{\boldsymbol{\xi}}_8 q_8} e^{\hat{\boldsymbol{\xi}}_9 q_9} \boldsymbol{g}_{st}(0) \tag{35}$$

$$\boldsymbol{g}_{st1}(q) = e^{\hat{\boldsymbol{\xi}}_1 q_1} e^{\hat{\boldsymbol{\xi}}_2 q_2} e^{\hat{\boldsymbol{\xi}}_3 q_3} e^{\hat{\boldsymbol{\xi}}_4 q_4} e^{\hat{\boldsymbol{\xi}}_5 q_5} e^{\hat{\boldsymbol{\xi}}_6 q_6} \boldsymbol{g}_{st1}(0) \tag{36}$$

B. INVERSE KINEMATICS OF THE ARM

1) INVERSE KINEMATIC OF ARM HOLDING THE SI

Based on (35), Equation (37) can be derived as:

$$\begin{aligned} & e^{\hat{\boldsymbol{\xi}}_4 q_4} e^{\hat{\boldsymbol{\xi}}_5 q_5} e^{\hat{\boldsymbol{\xi}}_6 q_6} e^{\hat{\boldsymbol{\xi}}_7 q_7} e^{\hat{\boldsymbol{\xi}}_8 q_8} \\ &= (e^{\hat{\boldsymbol{\xi}}_1 q_1} e^{\hat{\boldsymbol{\xi}}_2 q_2} e^{\hat{\boldsymbol{\xi}}_3 q_3})^{-1} \boldsymbol{g}_{st}(q) \boldsymbol{g}_{st}(0)^{-1} (e^{\hat{\boldsymbol{\xi}}_9 q_9})^{-1} \\ &= \boldsymbol{g}_1 e^{-\hat{\boldsymbol{\xi}}_9 q_9} \end{aligned} \tag{37}$$

First, both sides of (37) are multiplied by the intersection $\boldsymbol{p}_8$ between q_6, q_7, and q_8 axes. Second, the intersection $\boldsymbol{p}_5$ between q_4 and q_5 axes is subtracted from both sides of equation, and finally, the equation is solved.

$$\left\| (\boldsymbol{p}_8 - \boldsymbol{p}_5) \right\| = \left\| \boldsymbol{g}_1 e^{-\hat{\boldsymbol{\xi}}_9 q_9} \boldsymbol{p}_8 - \boldsymbol{p}_5 \right\| \tag{38}$$

q_9 can be determined.

And since q_9 is now known, Equation (37) yields

$$e^{\hat{\boldsymbol{\xi}}_4 q_4} e^{\hat{\boldsymbol{\xi}}_5 q_5} e^{\hat{\boldsymbol{\xi}}_6 q_6} e^{\hat{\boldsymbol{\xi}}_7 q_7} e^{\hat{\boldsymbol{\xi}}_8 q_8} = \boldsymbol{g}_1 e^{-\hat{\boldsymbol{\xi}}_9 q_9} \tag{39}$$

First, both sides of (39) are multiplied by $\boldsymbol{p}_9$. Second, the $\boldsymbol{p}_5$ is subtracted from both sides of equation, and the equation is solved

$$\left\| (e^{\hat{\boldsymbol{\xi}}_8 q_8} \boldsymbol{p}_9 - p_5) \right\| = \left\| \boldsymbol{g}_1 e^{-\hat{\boldsymbol{\xi}}_9 q_9} \boldsymbol{p}_9 - \boldsymbol{p}_5 \right\| \tag{40}$$

q_8 may be obtained using sub-problem 3. As q_8 and q_9 are known, Equation (37) yields

$$e^{\hat{\boldsymbol{\xi}}_4 q_4} e^{\hat{\boldsymbol{\xi}}_5 q_5} e^{\hat{\boldsymbol{\xi}}_6 q_6} e^{\hat{\boldsymbol{\xi}}_7 q_7} = \boldsymbol{g}_1 e^{-\hat{\boldsymbol{\xi}}_9 q_9} e^{-\hat{\boldsymbol{\xi}}_8 q_8} \tag{41}$$

Both sides of (41) are multiplied by the intersection $\boldsymbol{p}_8$ which yields

$$e^{\hat{\boldsymbol{\xi}}_4 q_4} e^{\hat{\boldsymbol{\xi}}_5 q_5} e^{\hat{\boldsymbol{\xi}}_6 q_6} e^{\hat{\boldsymbol{\xi}}_7 q_7} \boldsymbol{p}_8 = e^{\hat{\boldsymbol{\xi}}_4 q_4} e^{\hat{\boldsymbol{\xi}}_5 q_5} \boldsymbol{p}_8 = \boldsymbol{g}_1 e^{-\hat{\boldsymbol{\xi}}_9 q_9} e^{-\hat{\boldsymbol{\xi}}_8 q_8} \boldsymbol{p}_8 \tag{42}$$

q_4 and q_5 may be obtained using sub-problem 2.

As q_4, q_5, q_8 and q_9 are known, Equation (37) yields

$$e^{\hat{\boldsymbol{\xi}}_6 q_6} e^{\hat{\boldsymbol{\xi}}_7 q_7} = e^{-\hat{\boldsymbol{\xi}}_5 q_5} e^{-\hat{\boldsymbol{\xi}}_4 q_4} \boldsymbol{g}_1 e^{-\hat{\boldsymbol{\xi}}_9 q_9} e^{-\hat{\boldsymbol{\xi}}_8 q_8} \tag{43}$$

Both sides of (43) are multiplied by $\boldsymbol{p}_9$ to yield

$$e^{\hat{\boldsymbol{\xi}}_6 q_6} e^{\hat{\boldsymbol{\xi}}_7 q_7} \boldsymbol{p}_9 = e^{-\hat{\boldsymbol{\xi}}_5 q_5} e^{-\hat{\boldsymbol{\xi}}_4 q_4} \boldsymbol{g}_1 e^{-\hat{\boldsymbol{\xi}}_9 q_9} e^{-\hat{\boldsymbol{\xi}}_8 q_8} \boldsymbol{p}_9 = \boldsymbol{g}_4 \tag{44}$$

Now q_6 and q_7 may be obtained using sub-problem 2

2) INVERSE KINEMATICS OF THE ARM HOLDING THE ENDOSCOPE

Equation (36) becomes

$$e^{\hat{\boldsymbol{\xi}}_4 q_4} e^{\hat{\boldsymbol{\xi}}_5 q_5} e^{\hat{\boldsymbol{\xi}}_6 q_6} = e^{-\hat{\boldsymbol{\xi}}_3 q_3} e^{-\hat{\boldsymbol{\xi}}_2 q_2} e^{-\hat{\boldsymbol{\xi}}_1 q_1} \boldsymbol{g}_{st}(\theta) \boldsymbol{g}_{st1}(0)^{-1} = \boldsymbol{g}_5 \tag{45}$$

Both sides of (45) are multiplied by $\boldsymbol{p}_{\mathrm{r}}$ on the q_6 joint, which gives

$$e^{\hat{\boldsymbol{\xi}}_4 q_4} e^{\hat{\boldsymbol{\xi}}_5 q_5} e^{\hat{\boldsymbol{\xi}}_6 q_6} \boldsymbol{p}_r = e^{\hat{\boldsymbol{\xi}}_4 q_4} e^{\hat{\boldsymbol{\xi}}_5 q_5} \boldsymbol{p}_r = \boldsymbol{g}_4 \boldsymbol{p}_r = \boldsymbol{g}_5 \tag{46}$$

$$\begin{aligned} & \boldsymbol{p}_1 = \begin{bmatrix} 0 & 0 & 0 \end{bmatrix}^{\mathrm{T}}, \boldsymbol{p}_2 = \begin{bmatrix} 0 & a_1 & d_1 \end{bmatrix}^{\mathrm{T}}, \boldsymbol{p}_3 = \begin{bmatrix} 0 & a_1 + a_2 & d_1 \end{bmatrix}^{\mathrm{T}}, \\ & \boldsymbol{p}_4 = \boldsymbol{p}_5 = \boldsymbol{p}_6 = \boldsymbol{p}_7 = \begin{bmatrix} a_1 + a_2 + d_5 c_1 & 0 & d_1 - d_5 s_1 \end{bmatrix}^{\mathrm{T}}, \\ & \boldsymbol{p}_8 = \begin{bmatrix} a_1 + a_2 + d_5 c_1 - d_8 (s_1 s_3 - c_1 c_2 c_3) & -d_8 s_2 c_3 & d_1 - d_5 s_1 - d_8 (s_1 c_2 c_3 + c_1 s_3) \end{bmatrix}^{\mathrm{T}}, \\ & \boldsymbol{p}_9 = \begin{bmatrix} a_1 + a_2 + d_5 c_1 - (d_8 + d_9)(s_1 s_3 - c_1 c_2 c_3) & -(d_8 + d_9) s_2 c_3 & d_1 - d_5 s_1 - (d_8 + d_9)(s_1 c_2 c_3 + c_1 s_3) \end{bmatrix}^{\mathrm{T}} \end{aligned} \tag{29}$$

$$\boldsymbol{g}_{st}(0) = \begin{bmatrix} & a_1 + a_2 + d_5 c_1 + (d_8 + d_9 + d_{10})(c_1 c_2 c_3 - s_1 s_3) \\ I_{3\times 3} & -(d_8 + d_9 + d_{10}) s_2 c_3 \\ & d_1 - d_5 s_1 - (d_8 + d_9 + d_{10})(s_1 c_2 c_3 + c_1 s_3) \\ 0\ 0\ 0 & 1 \end{bmatrix} \tag{33}$$

$$\boldsymbol{g}_{st1}(0) = \begin{bmatrix} & a_1 + a_2 + d_5 c_{11} + d_8 (c_{11} c_2 c_3 - s_{11} s_3) \\ I_{3\times 3} & -d_8 s_2 c_3 \\ & d_1 - d_5 s_{11} - d_8 (s_{11} c_2 c_3 + c_{11} s_3) \\ 0\ 0\ 0 & 1 \end{bmatrix} \tag{34}$$

Now q_4 and q_5 can be determined by applying sub-problem 2. As q_4 and q_5 are known, q_6 can be obtained based on (46).

C. MASTER-SLAVE DESIGN

The master-slave control algorithm consisting of posture consistency control, incremental motion control and proportion motion control.

Posture consistency control comprises master motion control in display coordinate system (CS), arm motion control for holding SI in endoscopy CS, arm motion control for holding endoscopy in endoscope CS.

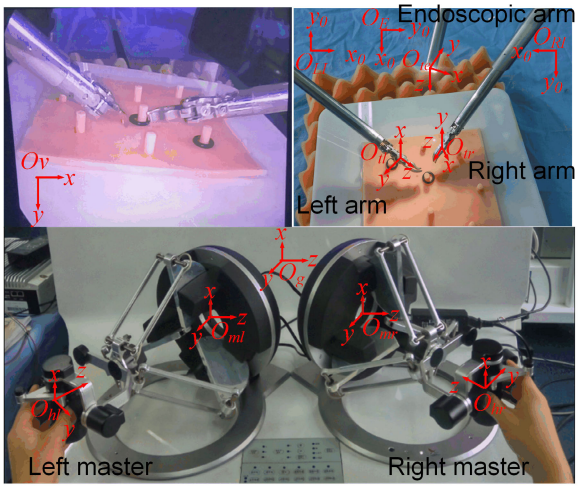

FIGURE 11. The definition of coordinate of MIS robot system.

1) ESTABLISHMENT OF THE MASTER-SLAVE CS

The master–slave CS is shown in Figure 11 including base CS (O_g -xyz), left master base CS (O_{ml}-xyz), right master base CS (O_{mr}-xyz), end-effector reference CS of left master (O_{hl}-xyz), end-effector reference CS of right master (O_{hr}-xyz), display CS (O_v-xyz), end-effector reference CS of endoscopy (O_{te}-xyz), end-effector reference CS of left arm holding SI (O_{tl}-xyz), end-effector reference CS of right arm holding SI (O_{tr}-xyz), base CS of the arm holding the endoscope (O_E-$x_0y_0z_0$), base CS of left arm holding the SI (O_{LI}-$x_0y_0z_0$), and base CS of right arm holding the SI (O_{RI}-$x_0y_0z_0$).

2) MASTER MOTION CONTROL IN THE DISPLAY CS

Master motion control in the display CS consists of end-effector position increment of master in Δt and end-effector absolute posture of master in $t+\Delta t$. The end-effector position and posture of master is described in (47), the position increment in Δt is given by (48), and the end-effector absolute posture of master in the display CS is expressed in (49).

$$\begin{aligned} {}^{O_V}_{O_{hl}}\boldsymbol{M} &= {}^{O_V}_{O_{ml}}\boldsymbol{R}\,{}^{O_{ml}}_{O_{hl}}\boldsymbol{T} \quad {}^{O_V}_{O_{hr}}\boldsymbol{M} = {}^{O_V}_{O_{mr}}\boldsymbol{R}\,{}^{O_{mr}}_{O_{hr}}\boldsymbol{T} \qquad (47)\\ {}^{O_V}_{O_{hl}}\Delta\boldsymbol{p} &= {}^{O_V}_{O_{ml}}\boldsymbol{R}\left({}^{O_{ml}}_{O_{hl}}\boldsymbol{p}_{t+\Delta t} - {}^{O_{ml}}_{O_{hl}}\boldsymbol{p}_t\right){}^{O_V}_{O_{hr}}\\ \Delta\boldsymbol{p} &= {}^{O_V}_{O_{mr}}\boldsymbol{R}\left({}^{O_{mr}}_{O_{hr}}\boldsymbol{p}_{t+\Delta t} - {}^{O_{mr}}_{O_{hr}}\boldsymbol{p}_t\right) \qquad (48)\end{aligned}$$

$$ {}^{O_V}_{O_{hl}}\boldsymbol{\omega}_{t+\Delta t} = {}^{O_V}_{O_{ml}}\boldsymbol{R}\,{}^{O_{ml}}_{O_{hl}}\omega_{t+\Delta t}\ {}^{O_V}_{O_{hr}}\boldsymbol{\omega}_{t+\Delta t} = {}^{O_v}_{O_{mr}}\boldsymbol{R}\,{}^{O_{mr}}_{O_{hr}}\boldsymbol{\omega}_{t+\Delta t} \qquad (49)$$

where ${}^{O_V}_{O_{hl}}\boldsymbol{M}$ and ${}^{O_V}_{O_{hr}}\boldsymbol{M}$ are the left and right end-effector position and posture of mater in display CS, respectively; ${}^{O_{ml}}_{O_{hl}}\boldsymbol{T}$ and ${}^{O_{mr}}_{O_{hr}}\boldsymbol{T}$ are the left and right end-effector position and posture in the base CS of left and right master, respectively; ${}^{O_V}_{O_{ml}}\boldsymbol{R}$ and ${}^{O_V}_{O_{mr}}\boldsymbol{R}$ are the transformation matrixes between left, right master and display CS, respectively; ${}^{O_{ml}}_{O_{hl}}\boldsymbol{\omega}_t$ and ${}^{O_{mr}}_{O_{hr}}\boldsymbol{\omega}_t$ are the left and right end-effector posture in the base CS of left and right master, respectively.

3) ARM MOTION CONTROL FOR HOLDING THE SI IN THE ENDOSCOPY CS

It is important in a variety of surgeries that the pincer motion of the SI is the same as the end-effector motion of the master, the end-effector position and posture changes according to the expectation of the surgeon.

When the local base CS of the endoscope arm is taken as the global base CS of the three arms. The end-effector position and posture of the arm holding the SI can be expressed as follows:

$$ {}^{O_{te}}_{O_{tl}}\boldsymbol{T} = \left({}^{O_E}_{O_{te}}\boldsymbol{T}\right)^{-1}{}^{O_E}_{O_{LI}}\boldsymbol{R}\,{}^{O_{LI}}_{O_{tl}}\boldsymbol{T}\,{}^{O_{te}}_{O_{tr}}\boldsymbol{T} = \left({}^{O_E}_{O_{te}}\boldsymbol{T}\right)^{-1}{}^{O_E}_{O_{RI}}\boldsymbol{R}\,{}^{O_{RI}}_{O_{tr}}\boldsymbol{T} \qquad (50)$$

where ${}^{O_{LI}}_{O_{tl}}\boldsymbol{T}$ and ${}^{O_{RI}}_{O_{tr}}\boldsymbol{T}$ are the position and posture of the end-effector CS (O_{tl}-xyz and O_{tr}-xyz) of the left and right arm holding SI in the local base CS (O_{LI}-$x_0y_0z_0$ and O_{RI}-$x_0y_0z_0$) of the left and right arm holding SI, respectively; ${}^{O_{te}}_{O_{tl}}\boldsymbol{T}$ and ${}^{O_{te}}_{O_{tr}}\boldsymbol{T}$ are the position and posture of the end-effector CS (O_{tl}-xyz and O_{tr}-xyz) of the left and right arm holding SI in base CS of arm holding endoscopy, respectively; ${}^{O_E}_{O_{LI}}\boldsymbol{R}$ and ${}^{O_E}_{O_{RI}}\boldsymbol{R}$ are the transformation matrixes between the local base CS (O_{LI}-$x_0y_0z_0$ and O_{RI}-$x_0y_0z_0$) of the left and right arm holding SI and the local cs of arm holding endoscopy, respectively; ${}^{O_E}_{O_{te}}\boldsymbol{T}$ is the position and posture of the end-effector CS (O_{te}-xyz) in the base CS (O_E-$x_0y_0z_0$) of arm holding endoscopy.

Where (α, β, γ, dx, dy, dz) is a set comprising the desired changes of position and posture of the master in the display CS. The desired end-effector position and posture of the SIs in the global base CS is given as follows:

$$ {}^{O_E}_{O_{tld}}\boldsymbol{T} = {}^{O_E}_{O_{te}}\boldsymbol{T}\boldsymbol{T}_d\,{}^{O_{te}}_{O_{tl}}\boldsymbol{T}\,{}^{O_E}_{O_{tr_d}}\boldsymbol{T} = {}^{O_E}_{O_{te}}\boldsymbol{T}\boldsymbol{T}_d\,{}^{O_{te}}_{O_{te}}\boldsymbol{T} \qquad (51)$$

The desired end-effector position and posture of the SIs in the local base CS of the arm holding the SI is obtained as follows:

$$ {}^{O_{LI}}_{O_{tld}}\boldsymbol{T} = \left({}^{O_E}_{O_{LI}}\boldsymbol{R}\right)^{-1}{}^{O_E}_{O_{tld}}\boldsymbol{T}\,{}^{O_{RI}}_{O_{trd}}\boldsymbol{T} = \left({}^{O_E}_{O_{RI}}\boldsymbol{R}\right)^{-1}{}^{O_E}_{O_{tr_d}}\boldsymbol{T} \qquad (52)$$

The desired end-effector position and posture change of the SIs in the local base CS of the arm fixing the SI is obtained as follows:

$$\Delta\boldsymbol{T}_{Ld} = {}^{O_{LI}}_{O_{tld}}\boldsymbol{T} - {}^{O_{LI}}_{O_{tli}}\boldsymbol{T}\,\Delta\boldsymbol{T}_{Rd} = {}^{O_{RI}}_{O_{trd}}\boldsymbol{T} - {}^{O_{RI}}_{O_{tri}}\boldsymbol{T} \qquad (53)$$

In order to verify the accuracy of arm motion control for holding the SI in the endoscopy CS, a hybrid simulation based

TABLE 5. The parameters of the arm fixing endoscopy.

q_1(mm)	q_2(rad)	q_3(rad)	d_5(mm)	a_1(mm)	a_2(mm)
1800	0.785	0.785	567	100	400

$r1$(rad)	α_1(rad)	α_2(rad)	q_4(rad)	q_5(rad)	q_6(mm)
0.22	1.29	0.99	0.7854	0.7854	100

TABLE 6. The parameters of the arm fixing SI.

q_1(mm)	q_2(rad)	q_3(rad)	d_5(mm)	a_1(mm)	a_2(mm)
1800	0.785	0.785	567	100	400

d_8(mm)	d_9(mm)	d_{10}(mm)	r_{11}(rad)	α_1(rad)	α_2(rad)
30	20	20	0.28	2.58	0.99

TABLE 7. The position and posture input parameters of the instrument manipulator based on endoscopic CS.

No.	a(°)	β(°)	γ(°)	dx(mm)	dy(mm)	dz(mm)
1	-5	5	5	20	-30	10

on Simulink and SimMechanics toolbox was performed. The desired end-effector position change of SI in the endoscopy CS was obtained by Simulink simulation based on (50), (51), (52), and (53). The actual end-effector position change of the SI in the endoscopy CS was obtained by SimMechanics simulation based on the initial passive joint values and each active joint value solved by inverse kinematics as input values. The input parameters of the arm holding endoscope and of the arm holding the SI are shown in Table 5 and Table 6 respectively. The input parameters of simulation are shown in Table 7. The desired end-effector position and posture change is [−0.0036 0.06174 0.03127 23.84; 0.0311 −0.1129 −0.0713 −56.94; 0.1323 0.05925 −0.0479 −179; 0 0 0 0]. The actual end-effector position and posture change is [−0.0036 0.06174 0.03127 23.84; 0.0311 −0.1129 −0.0713 −56.94; 0.1323 0.05925 −0.0479 −179; 0 0 0 0]. The desired end-effector position and posture change is equal to the actual end-effector position and posture change, which verifies the correctness of arm motion control for the arm holding the SI in the endoscopy CS.

4) ARM MOTION CONTROL FOR HOLDING THE ENDOSCOPE IN THE ENDOSCOPY CS

During surgery, the doctor may need to adjust the endoscope up/down, left/right, front/back according to the end-effector CS of endoscope. $\Delta \boldsymbol{p} = [dx, dy, dz, 1]^{\mathrm{T}}$ is defined as the position vector from the current field of view to the target field of view based on the end-effector CS of endoscopy. The absolute position of the target field of view based on the global base CS is given as

$$\begin{matrix} O_E \\ O_{te_d} \end{matrix} \Delta \boldsymbol{p} = \begin{matrix} O_E \\ O_{te} \end{matrix} \boldsymbol{T} \Delta \boldsymbol{p} \tag{54}$$

The initial endoscopic end position in the base CS of the arm holding the endoscope is $\begin{matrix} O_E \\ O_{tei} \end{matrix} \Delta \boldsymbol{p}$. The change to the desired end position in the base CS of the arm holding the endoscope is given as follows

$$\Delta \boldsymbol{p}_E = \begin{matrix} O_E \\ O_{ted} \end{matrix} \Delta \boldsymbol{p} - \begin{matrix} O_E \\ O_{tei} \end{matrix} \Delta \boldsymbol{p} \tag{55}$$

TABLE 8. The position vector of the objective window with respective to the current window.

NO	dx (mm)	dy(mm)	dz(mm)
1	27.56	35.76	43.89

In order to verify the correctness of arm motion control for the arm holding the endoscope in the endoscopy CS, a hybrid simulation based on Simulink and SimMechanics toolbox was performed. The desired end-effector position change of the endoscope in the endoscopy CS was obtained by Simulink simulation based (54) and (55). The actual end-effector position change of the endoscope in endoscopy CS was obtained by SimMechanics simulation based the initial passive joint values and each active joint value solved by inverse kinematics as input values. The input parameters of the arm holding the endoscope are shown in Table 5, the input parameters of simulation are shown in Table 8. The desired end-effector position change is [38.0317; 6.4633; 12.2014]. the actual end-effector position change is [38.0317; 6.4633; 12.2014]. The desired end-effector position change is equal to the actual end-effector position change, which verifies the correctness of arm motion control for the arm holding the endoscope in the endoscopy CS.

5) RELATIVE MOTION CONTROL

The position vectors of master and slave in the display CS are depicted as follows:

$$\begin{matrix} O_V \\ O_{ml} \end{matrix} R \left(\begin{matrix} O_{ml} \\ O_{hl} \end{matrix} \boldsymbol{p}_{t+1} - \begin{matrix} O_{ml} \\ O_{hl} \end{matrix} \boldsymbol{p}_t \right) = \left(\begin{matrix} O_E \\ O_{te} \end{matrix} \boldsymbol{T} \right)^{-1} \begin{matrix} O_E \\ O_{LI} \end{matrix} \boldsymbol{R} \left(\begin{matrix} O_{LI} \\ O_{tl} \end{matrix} \boldsymbol{p}_{t+1} - \begin{matrix} O_{LI} \\ O_{tl} \end{matrix} \boldsymbol{p}_t \right) \tag{56}$$

$$\begin{matrix} O_V \\ O_{mr} \end{matrix} R \left(\begin{matrix} O_{mr} \\ O_{hr} \end{matrix} \boldsymbol{p}_{t+1} - \begin{matrix} O_{mr} \\ O_{hr} \end{matrix} \boldsymbol{p}_t \right) = \left(\begin{matrix} O_E \\ O_{te} \end{matrix} \boldsymbol{T} \right)^{-1} \begin{matrix} O_E \\ O_{RI} \end{matrix} \boldsymbol{R} \left(\begin{matrix} O_{RI} \\ O_{tr} \end{matrix} \boldsymbol{p}_{t+1} - \begin{matrix} O_{RI} \\ O_{tr} \end{matrix} \boldsymbol{p}_t \right) \tag{57}$$

where $\begin{matrix} O_{ml} \\ O_{hl} \end{matrix} \boldsymbol{p}_t$ and $\begin{matrix} O_{mr} \\ O_{hr} \end{matrix} \boldsymbol{p}_t$ are the position vectors of the end-effector CS (O_{hl}-xyz and O_{hr}-xyz) in the left and right master base CS, respectively. $\begin{matrix} O_{LI} \\ O_{tl} \end{matrix} \boldsymbol{p}_t$ and $\begin{matrix} O_{RI} \\ O_{tr} \end{matrix} \boldsymbol{p}_t$ are the position vectors of the end-effector CS (O_{tl}-xyz and O_{tr}-xyz) in the left and right base CS (O_{LI}-$x_0y_0z_0$ and O_{RI}-$x_0y_0z_0$) of arm fixing SI, respectively.

The relative motion control is suitable for position control and is not suitable for posture control, in order to maintain the consistency of master-salve control, the absolute posture control is given as follows:

$$\begin{matrix} O_v \\ O_{ml} \end{matrix} \boldsymbol{R} \begin{matrix} O_{ml} \\ O_{hl} \end{matrix} \boldsymbol{\omega} = \left(\begin{matrix} O_E \\ O_{te} \end{matrix} \boldsymbol{T} \right)^{-1} \begin{matrix} O_E \\ O_{LI} \end{matrix} \boldsymbol{R} \begin{matrix} O_{LI} \\ O_{tl} \end{matrix} \boldsymbol{\omega}$$

$$\begin{matrix} O_v \\ O_{mr} \end{matrix} \boldsymbol{R} \begin{matrix} O_{mr} \\ O_{hr} \end{matrix} \boldsymbol{\omega} = \left(\begin{matrix} O_E \\ O_{te} \end{matrix} \boldsymbol{T} \right)^{-1} \begin{matrix} O_E \\ O_{RI} \end{matrix} \boldsymbol{R} \begin{matrix} O_{RI} \\ O_{tr} \end{matrix} \boldsymbol{\omega} \tag{58}$$

where $\begin{matrix} O_{ml} \\ O_{hl} \end{matrix} \boldsymbol{\omega}_t$ and $\begin{matrix} O_{mr} \\ O_{hr} \end{matrix} \boldsymbol{\omega}_t$ are the posture vectors of the end-effector CS (O_{hl}-xyz and O_{hr}-xyz) in the left and right master base CS, respectively. $\begin{matrix} O_{LI} \\ O_{tl} \end{matrix} \boldsymbol{\omega}_t$ and $\begin{matrix} O_{RI} \\ O_{tr} \end{matrix} \boldsymbol{\omega}_t$ are the posture vectors of the end-effector CS (O_{tl}-xyz and O_{tr}-xyz) in the left and

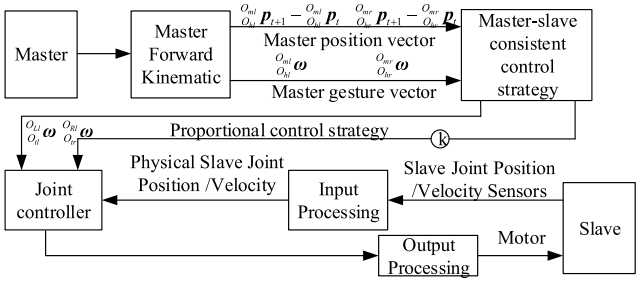

FIGURE 12. The master-slave motion algorithm consisting of three control strategies.

right base CS (O_{LI}-$x_0y_0z_0$ and O_{RI}-$x_0y_0z_0$) of arm fixing SI, respectively.

6) SCALE MOTION CONTROL

In order to meet the needs of different types of operation, we designed a master–slave mapping proportion control strategy with 1:1, 3:1, and 5:1. For example, in order to reduce the slave motion and improve the operation accuracy when a blood vessel is sutured and knotted, the proportion can be set as 5:1. The scale motion control should meet the requirement of master–slave control consistency. The scale motion control is given as follows

$$\begin{aligned} &{}^{O_v}_{O_{ml}}R\left({}^{O_{ml}}_{O_{hl}}\boldsymbol{p}_{t+1}-{}^{O_{ml}}_{O_{hl}}\boldsymbol{p}_t\right)/k \\ &\quad=\left({}^{O_E}_{O_{te}}\boldsymbol{T}\right)^{-1}{}^{O_E}_{O_{LI}}\boldsymbol{R}\left({}^{O_{LI}}_{O_{tl}}\boldsymbol{p}_{t+1}-{}^{O_{LI}}_{O_{tl}}\boldsymbol{p}_t\right) \end{aligned} \tag{59}$$

$$\begin{aligned} &{}^{O_v}_{O_{mr}}R\left({}^{O_{mr}}_{O_{hr}}\boldsymbol{p}_{t+1}-{}^{O_{mr}}_{O_{hr}}\boldsymbol{p}_t\right)/k \\ &\quad=\left({}^{O_E}_{O_{te}}\boldsymbol{T}\right)^{-1}{}^{O_E}_{O_{RI}}\boldsymbol{R}\left({}^{O_{RI}}_{O_{tr}}\boldsymbol{p}_{t+1}-{}^{O_{RI}}_{O_{tr}}\boldsymbol{p}_t\right) \end{aligned} \tag{60}$$

The scale motion control is suitable for position control but is not suitable for posture control. Hence, the posture control requirement should be satisfied using (58).

The master–slave control strategy including master–slave motion consistency, relative motion control, and scale motion control is shown in Figure 12.

VI. AUXILIARY CONTROL STRATEGY

A. MASTER-SLAVE POSTURE REGISTRATION

Relative position motion control is used, and the initial position of the SI does not affect the position control. However, the posture of the SI should be consistent with the gesture of the master. The posture of the SI relative to the master should be pre-registered when the SI is installed. There are two methods to achieve registration. The first involves adjusting the posture of the master to be consistent with the gestures of the SI, while the posture of the SI remains unchanged. The second involves adjusting the gestures of the SI to be consistent with the posture of the master, while the posture of the master remains unchanged. The second method was applied because the master wrist has no motor and is therefore passive.

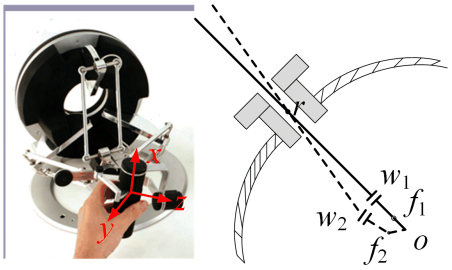

FIGURE 13. The schematic diagram of Master-slave posture Registration.

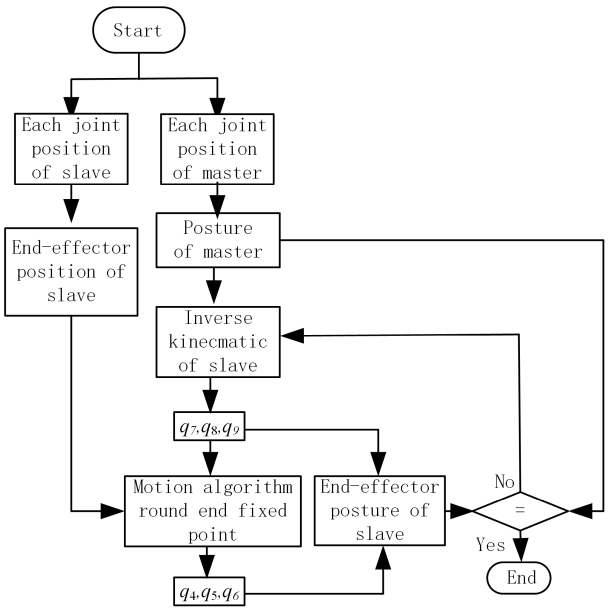

FIGURE 14. Program flow chart.

There are two ways to carry out the second method. The first is to adjust the gestures of the SI to be consistent with the posture of the master when the wrist position of the SI remains unchanged. The second is to adjust the gestures of the SI to be consistent with the posture of the master when the end-effector position of the SI remains unchanged. The end-effector of the SI must remain spatially unchanged, to prevent destruction of the tissue. In limited cases, the connection between wrist and forceps may compress the tissue. However, because the structure of the connection is not as sharp as the tip of the end-effector of SI, this will not cause tissue damage, and the safety of this approach is relatively high. In Figure 13 the solid line indicates the position where the SI is inserted, and the dotted line is the same as the posture of the master after the instrument is registered.

Detailed implementation procedures are shown in Figure 14. First, information on the joint position of the master and slave is collected. The posture of the master in the display CS and the spatial position of the SI are calculated based on the forward kinematics. The three DOFs (q_7, q_8, and q_9) of the SI can be determined based on the calculated values of the three joint positions (q_4, q_5, and q_6) of the RCM mechanism, and the posture information derived from

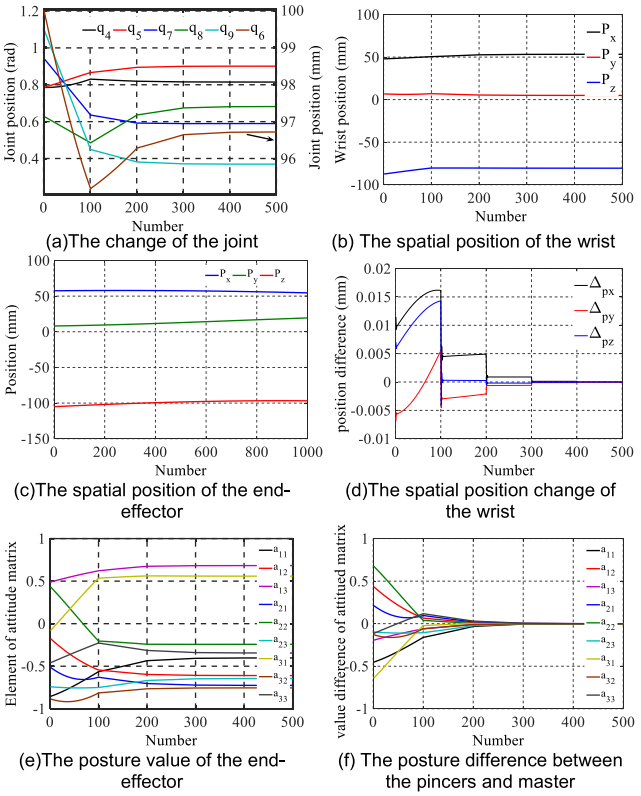

FIGURE 15. Simulation result.

the master and slave inverse kinematics. In order to keep the forceps spatial position unchanged, the three joint position values (q_7, q_8, and q_9) are substituted into the algorithm used to keep the end-effector unchanged. Values for the three DOF joint positions (q_4, q_5, and q_6) of the RCM mechanism are calculated, and the active joint position values (q_4, q_5, q_6, q_7, q_8, and q_9) are substituted into the forward kinematics.

If the posture between the SI and master is not consistent, the three DOFs (q_7, q_8, and q_9) of the SI can be deduced based on three joint position values (q_4, q_5, and q_6) of the RCM mechanism, and the posture information of the master and slave inverse kinematics. In order to keep the end-effector spatial position unchanged, the three joint position values (q_7, q_8, and q_9) are substituted into the algorithm used to keep the end-effector unchanged. The three DOF joint position values (q_4, q_5, and q_6) of the RCM mechanism are calculated, and the active joint position values (q_4, q_5, q_6, q_7, q_8, and q_9) are substituted into the forward kinematics.

If the posture between the SI and the master is not consistent, the above calculation procedure is repeated until the posture between the master and the end-effector of the SI is consistent.

The simulation experiment was used to confirm that the above algorithm is correct and effective. The posture information of the master is obtained as shown in (61). The position of the end-effector of the SI is collected as shown in (62). The active joint initial position is shown in Table 9. The simulation results are shown in Figure 15. The position change of the

TABLE 9. Input parameters used in the simulation.

Input parameters					
q_4 /rad	q_5/rad	q_6/mm	q_7/rad	q_8/rad	q_9/rad
0.25π	0.25π	100	0.3π	0.2π	0.35π

end-effector of the SI was very small, and the error was less than 0.01 and hence negligible. The posture between master and the SI was consistent after multiple iterations, the errors between the elements of the posture matrix were less than 0.0001 and therefore negligible.

$$\boldsymbol{\omega} = \begin{bmatrix} -0.4025 & -0.6098 & 0.6827 \\ -0.7255 & -0.2423 & -0.6442 \\ 0.5583 & -0.7546 & -0.3449 \end{bmatrix} \tag{61}$$

$$\boldsymbol{p} = \begin{bmatrix} 42.3650 & -11.7931 & -109.3960 \end{bmatrix}^{\mathrm{T}} \tag{62}$$

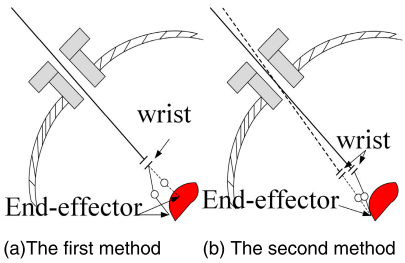

FIGURE 16. The schematic diagram of surgery instrument replacement.

B. SI REPLACEMENT STRATEGY

A variety of SIs are used in MIS, and corresponding SI exchange strategies are necessary to ensure safe and quick replacement of SIs. The three joints of the SI should return to the initial position, before the SI can safely be removed from the trocar. There are two methods by which this may be achieved. In the first, most direct method, the three joints are rotated directly to the initial position [Figure 16 (a)]. The second method involves rotating the three joints to the initial position while keeping the position of the end-effector of the SI unchanged [Figure 16 (b)]. The second method is preferred, as it causes no damage to the tissue. In limited cases, the connection between the wrist and forceps may compress the tissue. However, because the structure of the connection is not as sharp as the tip of the SI, it will not cause tissue damage. Hence, the safety of this approach is relatively high. The corresponding calculation procedures are shown in Figure 17. The joint position information of the RCM mechanism is collected and the end-effector positions of the SIs calculated based on forward kinematics.

Supposing that the above zeroing work is completed by n steps. In the ith step, the positions of q_7, q_8, and q_9 joints are shown in (63). In the i-1 step, the positions of the q_4, q_5, and q_6 joints are $q_{4(i-1)}$, $q_{5(i-1)}$ and $q_{6(i-1)}$. The positions of the wrist ($p_{xw(i)}$, $p_{yw(i)}$, $p_{zw(i)}$) and the end-effectors of the SIs ($p_{xm(i)}$, $p_{ym(i)}$, $p_{zm(i)}$) are calculated based on forward kinematics. The relationship between wrist and forceps of the SI is given by (64).

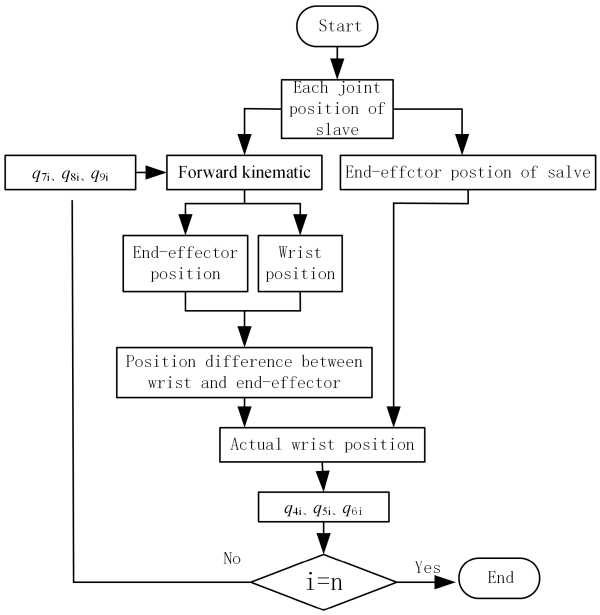

FIGURE 17. Program flow chart.

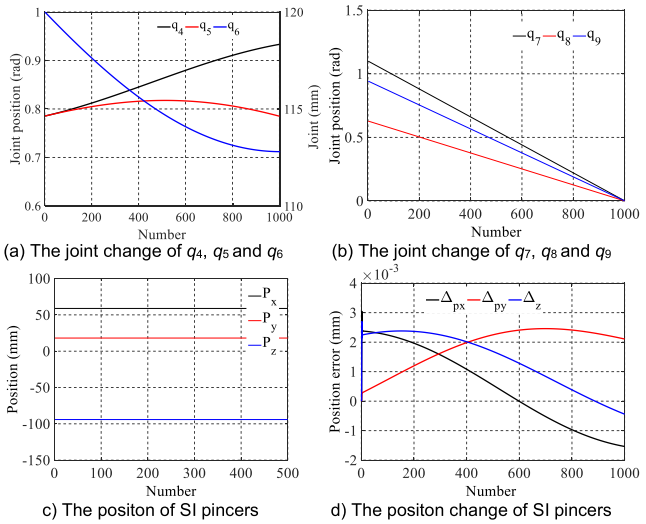

FIGURE 18. The simulation of movement around the fixed point.

In order to keep the position of the forceps unchanged when the joints (q_7, q_8, and q_9) return to their original positions, the position of compensation in the wrist is calculated for the end-effector position change of the SI as shown in (65). The joint positions (q_4, q_5, and q_6) can be calculated based on inverse kinematics. When the nth step is completed, the joints (q_7, q_8, and q_9) return to their initial positions, and the SI may be extracted.

Motion simulation around a fixed point is used to validate the above algorithm in terms of accuracy and effectiveness. The simulation set is shown in Table 10. The simulation results are shown in Figure18. The error was less than 0.004 mm and therefore negligible. (63)–(66), as shown at the bottom of the page.

TABLE 10. Input parameters used in the simulation.

Input parameters					
q_4 /rad	q_5/rad	q_6/mm	q_7/rad	q_8/rad	q_9/rad
0.25π	0.25π	120	0.25π	0.25π	0.25π

VII. EXPERIMENTS AND RESULTS

A. EXPERIMENTS TO VERIFY THE EFFECTIVENESS OF TWO DECOUPLING METHODS

1) EXPERIMENT TO VERIFY THE FIRST DECOUPLING METHOD

The experiments were carried out to test the angle variation of pincer movement caused by the coupling motion between wrist and forceps, applying the Optotrak certus system. Three markers were used to record the positions of the two forceps and wrist as shown in Figure 19. The length from Marker 1 to Marker 2 is represented by a, where Δa reflects the angle variation of pincer movement caused by the coupling motion between wrist and forceps. The length between Marker 1 and Marker 3 is represented as b, and c is the length between Marker 2 and Marker 3. The wrist movement is set as $0^\circ \sim 90^\circ \sim 0^\circ \sim -90^\circ \sim 0^\circ$. Figure 20 shows Δa, Δb, and Δc. $|\Delta a| < 0.06$ mm, rotational angle of pincer movement caused by the coupling motion is less than 0.09° (the pincer length is 20 mm). Δa is very small and does not influence the position of the forceps. Δb and Δc indicate the effects on the wire cable pretension between forceps and wrist and may affect the pincer posture. However, $\Delta b < 0.07$ mm and $\Delta c < 0.06$ mm, which are very small and hence do not affect the surgeon's ability to operate.

2) EXPERIMENT TO VERIFY THE SECOND DECOUPLING METHOD

The experiment was performed to test the angle variation of four rotatory interface disks of the SI caused by the coupling motion between rotational motion (S_1, S_2, S_3, and S_4 in Figure 21) and the translational motion (S_5 in Figure 21) of

$$q_{7i} = q_{70} - (i/n)\, q_{70}\ q_{8i} = q_{80} - (i/n)\, q_{80}\ q_{9i} = q_{90} - (i/n)\, q_{90} \tag{63}$$

$$\boldsymbol{l} = \left[p_{\mathrm{wx}} - p_{mx} \quad p_{\mathrm{wy}} - p_{my} \quad p_{\mathrm{wz}} - p_{mz} \right]^{\mathrm{T}} \tag{64}$$

$$\boldsymbol{p}_t = \left[p_{\mathrm{wx(i)}} - p_{mx(\mathrm{i})} + p_{mx} \quad p_{\mathrm{wy(i)}} - p_{my(\mathrm{i})} + p_{my} \quad p_{\mathrm{wz(i)}} - p_{mz(\mathrm{i})} + p_{mz} \right] \tag{65}$$

$$\Delta q_6 = \sqrt{\left(p_x^t - p_x^O\right)^2 + \left(p_y^t - p_y^O\right)^2 + \left(p_z^t - p_z^O\right)^2} - l_1 - l_2 - q_6^t \tag{66}$$

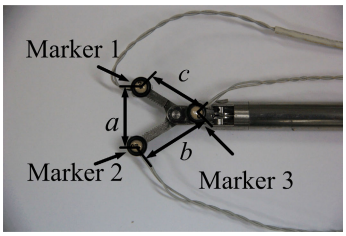

FIGURE 19. The experiment to test the angle variation of pincer movement.

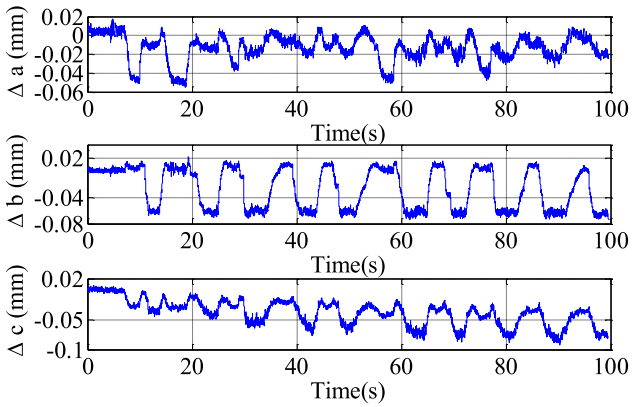

FIGURE 20. The length changes of *a*, *b* and *c*.

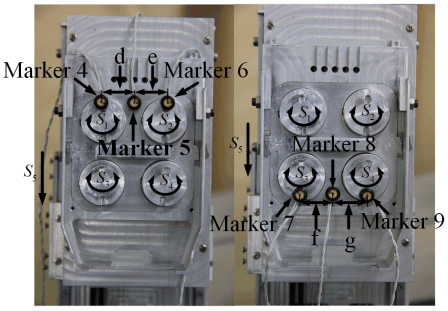

FIGURE 21. The experiment to test coupling motion.

the mobile platform. Six markers (Marker 4, 5, 6, 7, 8, and 9) were installed on interface disk S_1, isolation board, interface disk S_2, interface disk S_3, isolation board and interface disk S_4, respectively, to record the positions of S_1, S_2, S_3, S_4, and isolation board as shown in Figure 21. The lengths between Markers 4, 6 and 5, are d and e respectively. The lengths between Markers 7, 9 and 8 are f and g, respectively. The change in length is expressed by (67) and represents the coupling motion. The movement process of the mobile platform is set as 0 mm $\sim$ 310 mm $\sim$ 0 mm $\sim$ 310 mm. The test results are shown in Figure 22 as $\Delta d < 0.01$ mm, $\Delta e < 0.015$ mm, $\Delta f < 0.03$ mm, and $\Delta g < 0.02$ mm, which means that the angle variations of four rotatory interface disks of the SI are 0.06°, 0.09°, 0.17°, and 0.1°, respectively (the diameters of S_1, S_2, S_3, and S_4 are 20 mm). These changes are very small and probably caused by differential pretension forces, machining and assembly errors.

$$\Delta d = d_t - d_0 \quad \Delta e = e_t - e_0 \; \Delta f = f_t - f_0 \Delta g = g_t - g_0 \tag{67}$$

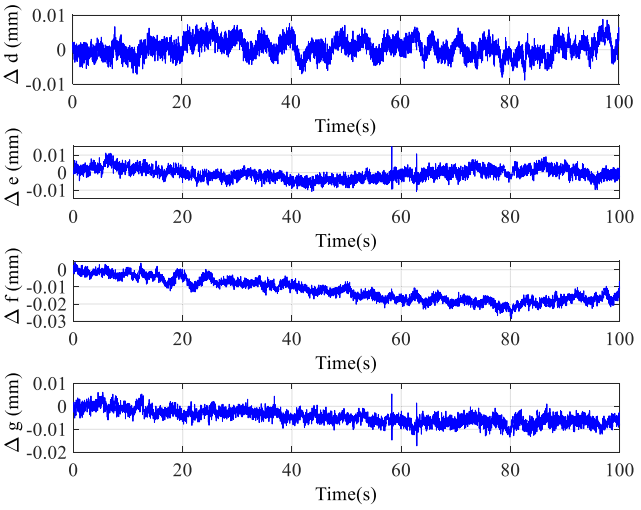

FIGURE 22. The test results.

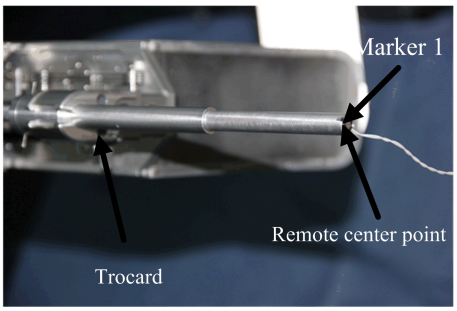

FIGURE 23. The experiment to test the change in the position of the fixing point.

where d_t, e_t, f_t and g_t are the lengths of the d, e, f and g at time t, d_0, e_0, f_0 and g_0 are the lengths of the d, e, f and g at time 0, respectively.

B. EXPERIMENT TO TEST THE PERFORMANCE INDICES OF MIS ROBOT

1) EXPERIMENT TO TEST THE POSITION CHANGE OF THE FIXING POINT OF THE SPHERICAL RCM MECHANISM

Marker 1 is installed to record the position of the fixing point as shown in Figure 23. The rotation process of joint 1 in the spherical RCM mechanism is 0 ° $\sim$ 90 ° $\sim$ 0 ° $\sim$ 90 ° $\sim$ 0 °. The rotation process of joint 2 in the spherical RCM mechanism is 0 ° $\sim$ 90 ° $\sim$ 165 ° $\sim$ 90 ° $\sim$ 0 °. The definition of the fixing point spatial position change is given by (68). Figure 24 shows $\Delta x < 0.5$ mm, $\Delta y < 0.65$ mm, $\Delta z < 0.6$ mm. The change in position of the fixing point occurs within a spherical area with a diameter of 1.6 mm, which is within the elastic deformation range of epidermal tissue and thus does not destroy epidermal tissue.

$$\Delta x_{\mathrm{i}} = x_i - \frac{1}{n}\sum_{j=1}^{n} x_j \quad \Delta y_{\mathrm{i}} = y_i - \frac{1}{n}\sum_{j=1}^{n} y_j$$

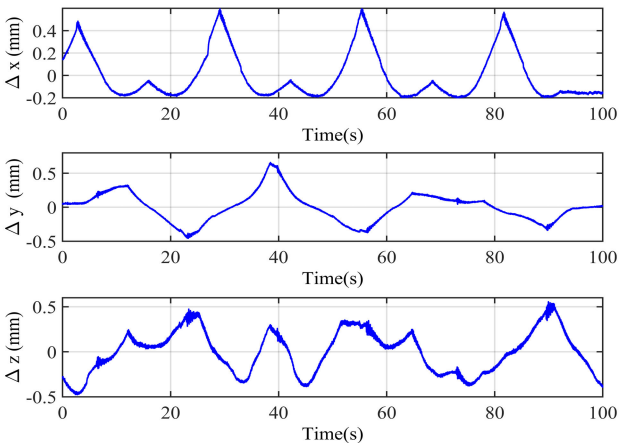

FIGURE 24. The change in the position of the fixing point.

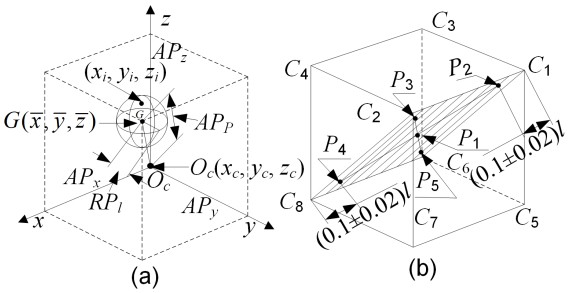

FIGURE 25. (a) The definition of positioning accuracy and repeating positioning accuracy; (b) The cube and test points.

$$\Delta z_{\mathrm{i}} = z_i - \frac{1}{n}\sum_{j=1}^{n} z_j$$
$$R_p = \max\{\sqrt{(\Delta x_i)^2 + (\Delta y_i)^2 + (\Delta z_i)^2}\} \tag{68}$$

2) MIS ROBOT POSITIONING AND REPEATED POSITIONING ACCURACY TEST

The MIS robot positioning and repeated positioning accuracy test was conducted using the Optotrak certus system. Based on ISO 9283:1998, the positioning accuracy is shown in Figure 25 (a) and expressed as

$$AP_P = \sqrt{(\bar{x} - x_c)^2 + (\bar{y} - y_c)^2 + (\bar{z} - z_c)^2},$$
$$\bar{x} = \frac{1}{n}\sum_{j=1}^{n} x_j, \bar{y} = \frac{1}{n}\sum_{j=1}^{n} y_j,$$
$$\bar{z} = \frac{1}{n}\sum_{j=1}^{n} z_j, AP_x = \bar{x} - x_c, AP_y = \bar{y} - y_c, AP_z = \bar{z} - z_c \tag{69}$$

Repeated positioning accuracy is shown in Figure 25 (a) and expressed as

$$RP_l = \bar{l} + 3S_l, l_a = \frac{1}{n}\sum_{i=1}^{n} l_i,$$

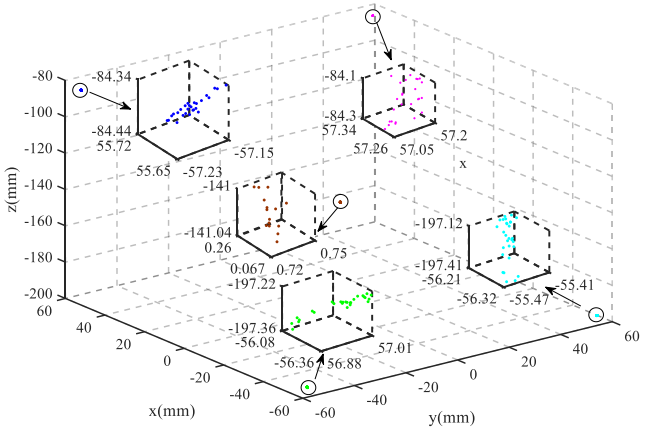

FIGURE 26. The 30 experiment results.

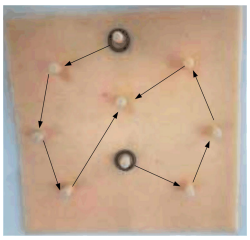

FIGURE 27. The trajectory of collar experiment.

$$l_i = \sqrt{(x_i - \bar{x})^2 + (y_i - \bar{y})^2 + (z_i - \bar{z})^2},$$
$$\bar{x} = \frac{1}{n}\sum_{j=1}^{n} x_j, \quad \bar{y} = \frac{1}{n}\sum_{j=1}^{n} y_j,$$
$$\bar{z} = \frac{1}{n}\sum_{j=1}^{n} z_j S_l = \sqrt{\sum_{j=1}^{n} (l_i - l_a)/n - 1} \tag{70}$$

Referring to ISO 9283:1998, five points are located in the cube, which has the maximum volume allowable with the edges parallel to the base CS. Figure 25 (b) is applied to test the positioning and repeated positioning accuracy. The $C_1C_2C_6C_8$ plane with five test points (P_1, P_2, P_3, P_4, and P_5) is the test plane. The C_1, C_2, C_6, C_8, P_1, P_2, P_3, P_4, and P_5 positions are shown in Table 11. The test path of 30 repeated experiments is $P_1 \rightarrow P_2 \rightarrow P_3 \rightarrow P_4 \rightarrow P_5 \rightarrow P_1$, the corresponding test results are shown in Figure 26. The corresponding positioning and repeated positioning accuracy are shown in Tables 12 and 13, respectively. The minimum positioning and repeated positioning accuracy of the MIS robot are 1.40 mm and 0.25 mm, respectively.

C. EXPERIMENT TO VERIFY THE MASTER-SLAVE COTROL ALGORITHM

Collar and threading tests were used to validate the accuracy and efficiency of the master–slave control algorithm. In order to make these validations simultaneously, the requirements of the collar and threading tests for the mast–slave control algorithm were high.

TABLE 11. The position of points depicted in Figure 29.

Symbol	x-coordinate	y-coordinate	z-coordinate
C_1	-70.71	70.71	-70.71
C_2	70.71	-70.71	-70.71
C_6	-70.71	-70.71	-212.13
C_8	70.71	-70.71	-212.13
P_1	0	0	-141.42
P_2	56.57	56.57	-84.85
P_3	56.57	-56.57	-84.85
P_4	-56.57	-56.57	-197.99
P_5	-56.57	56.57	-197.99

TABLE 12. Positioning accuracy of five points.

	P_1	P_2	P_3	P_4	P_5
AP_x	0.73	0.61	0.58	0.40	1.14
AP_y	0.16	0.89	0.72	0.32	0.32
AP_z	0.41	0.49	0.65	0.82	0.75
AP	0.89	1.18	1.13	0.97	1.40

TABLE 13. Repeated position accuracy of five test points.

	P_1	P_2	P_3	P_4	P_5
L_A	0.05	0.03	0.08	0.09	0.08
S_L	0.02	0.02	0.04	0.05	0.05
RP_L	0.13	0.10	0.21	0.25	0.24

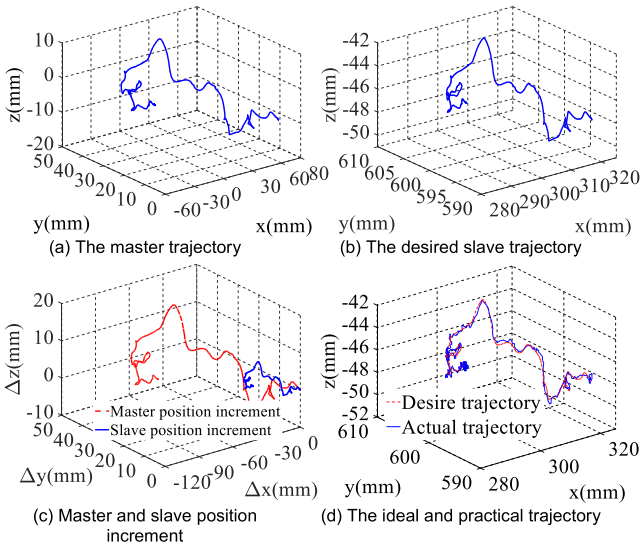

FIGURE 28. Trajectory tracking experiment of the master-slaver control algorithm.

1) COLLAR EXPERIMENT

The settings of the collar experiment were 4 mm column diameter, 7 mm collar diameter, operational panel fixed on the table, and two SIs used to clamp collars in place on the column. The operational trajectory is shown in Figure 27. The partial trajectories of the master and slave during experiment were collected, and the desired trajectory of the slave calculated based on the master–slave control algorithm. The related trajectory is shown in Figure 28 a) and b). The slave trajectory followed the master trajectory. The absolute position of the slave and master was not consistent, and the incremental position control was realized. The position increments of the master and slave are shown in Figure 28 c). The movement trend between master and slave was consistent. Because the scale was set at 3:1, the master position increment was greater than the slave position increment, and proportional control was achieved. The desired joint position of the slave can be calculated based on slave inverse kinematics and the master trajectory. The desired trajectory of the slave can be obtained based on forward kinematics. The actual trajectory of slave can be calculated based on the actual joint position and forward kinematics. The desired and actual trajectories of the slave are shown in Figure 28 d). This indicates that the slave follows the trajectory of master, reproducing the surgeon's hand trajectory and successfully completing the operation.

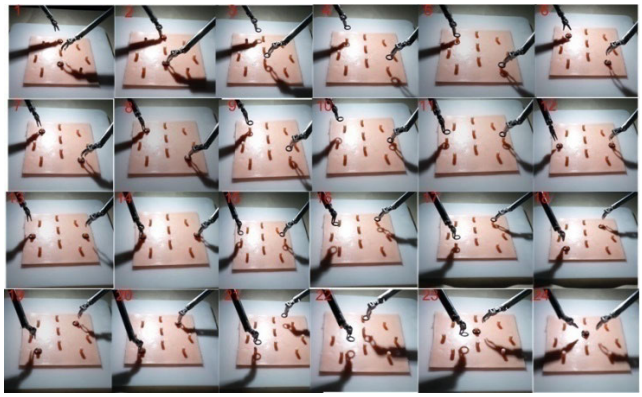

FIGURE 29. Collar experiment.

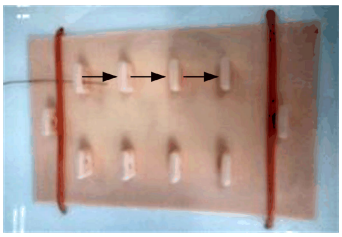

FIGURE 30. The trajectory of threading experiment.

The actual operation experiment of operators was used to verify the consistency of the master-slave attitude. The doctor operated two masters to control the slave to realize the collar experiment, the experiment process is shown in Figure 29, it can be seen that the loop was successfully placed on the column by the SIs, the master-slave attitude consistency motion control was realized. This collar experiment verifies the correctness and effectiveness of the master-slave control algorithm for the MIS robot.

2) THREADING EXPERIMENT

The settings of the threading experiment were a 4 mm hole diameter, 0.5 mm thread diameter, the operational panel fixed on the table, and two SIs hold the suture to complete the threading. The operational trajectory is shown in Figure 30.

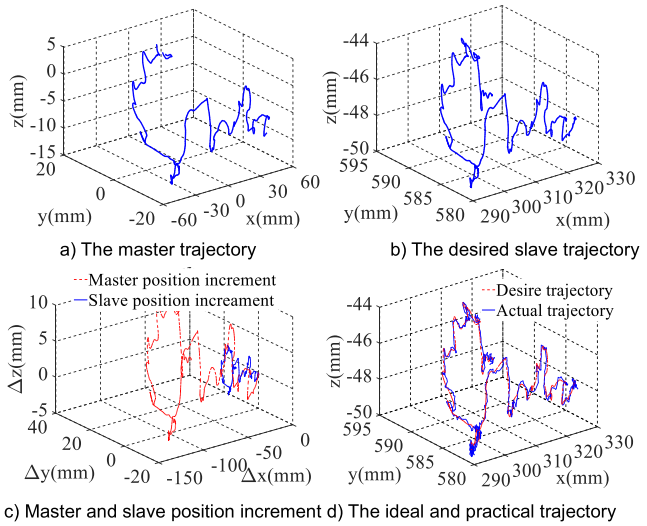

FIGURE 31. Trajectory tracking experiment of the master-slaver control algorithm.

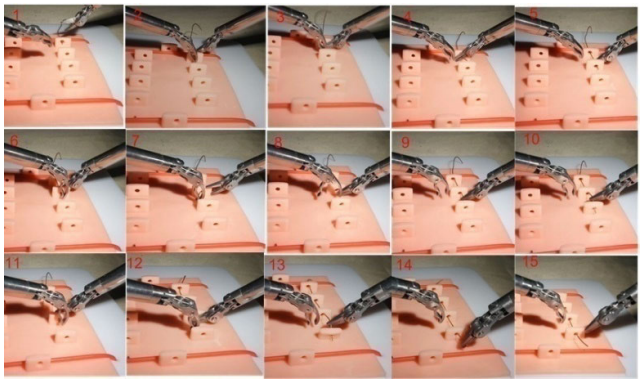

FIGURE 32. Threading experiment.

The partial trajectories of the master and slave during the experiment were collected, and the desired trajectory of the slave calculated based on the master–slave control algorithm. The related trajectory is shown in Figure 31 a) and b). The slave trajectory followed the master trajectory. The absolute position of the slave and master was not consistent, however incremental position control was achieved. The incremental positions of the master and slave are given in Figure 31 c). The movement trend between master and slave was consistent. Because the scale was set as 3:1, the master position increment was greater than the slave position increment, and proportional control was achieved. The desired joint position of the slave can be calculated based on the slave inverse kinematics and the master trajectory. The desired trajectory of the slave can be obtained based on the forward kinematic. The actual trajectory of the slave can be calculated based on the actual joint position and the forward kinematics. The desired and actual trajectories of the slave are shown in Figure 31 d). In conclusion, the slave follows the trajectory of the master, reproduces the doctor's hand trajectory and completes the operation.

FIGURE 33. Cholecystectomy experiment.

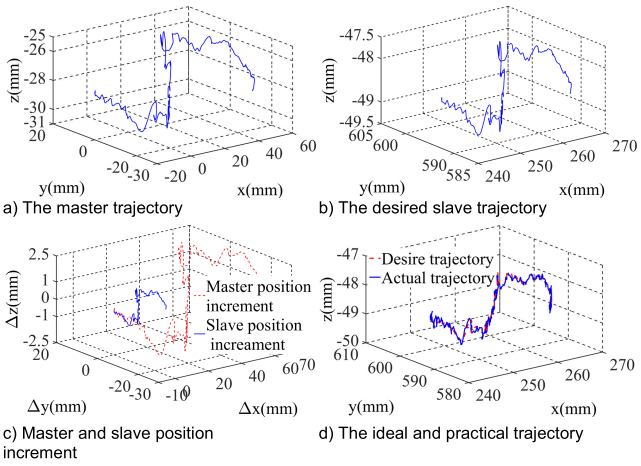

FIGURE 34. Trajectory tracking experiment of the master-slaver control algorithm.

The actual operation experiment of operators was used to verify the consistency of the master-slave attitude. The doctor operated two masters to control the slave to realize the threading experiment, the experiment process is shown in Figure 32, it can be seen that the threading was successfully passed through the hole by the SIs, the master-slave attitude consistency motion control was realized. This threading experiment verifies the correctness and effectiveness of the master-slave control algorithm for the MIS robot.

D. ANIMAL EXPERIMENTS

1) CHOLECYSTECTOMY EXPERIMENT

The validity of the entire MIS robot system was verified by animal experiments. A cholecystectomy was performed on

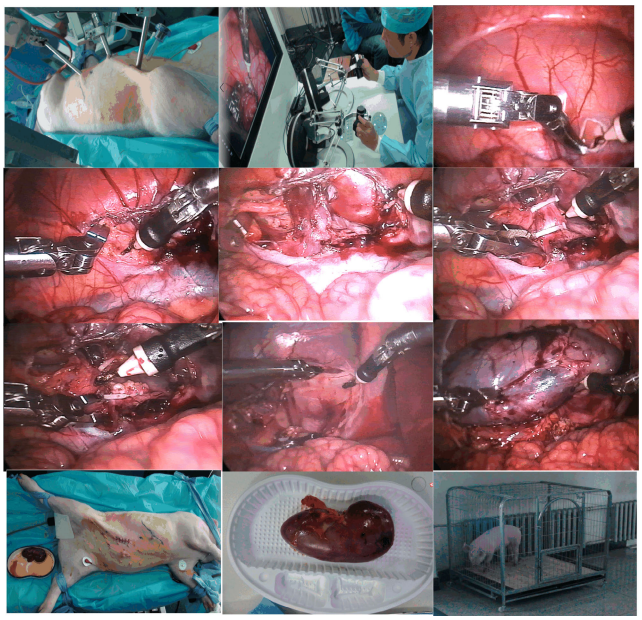

FIGURE 35. Nephrectomy experiment.

TABLE 14. The error between the ideal and practical trajectory.

	x	y	z	3-D
Max error (mm)	0.5933	0.6406	0.5493	0.7531
Average error(mm)	0.1559	0.1414	0.1407	0.2535

a 35 kg pig. The time taken for preoperational preparation was about 30 min. The entire surgical process is shown in Figure 33. It took about 30 min to complete the surgery and only 15 ml of blood was lost. The pig revived 40 min after surgery, and walked 10 min later. It started eating 8 hours post-surgery. The pig's survival and good health indicate that the performance indices of the MIS robot (decoupling motion, accuracy of the fixed point, positioning accuracy and repeated positioning accuracy) meet the surgical requirements without causing damage to tissues or organs. The small amount of bleeding also indicates that the robot is well controlled and has high dexterity.

The partial trajectories of the master and slave were collected during the experiment, and the desired trajectory of the slave was calculated based on the master–slave control algorithm. The master and desired slave trajectories are shown in Figure 34 a) and b). The slave trajectory followed the master trajectory. Since the proportional control factor was set to 3:1, the master position increment was greater than the slave position increment as shown in Figure 34 c), however, the movement trend between master and slave was consistent. Based on the joint positions collected for the slave manipulator and forward kinematics of slave, the actual trajectory may be calculated as shown in Figure 34 d). The slave follows the desired trajectory well. The error between the desired trajectory and actual trajectory of slave is shown in Table 14. The maximum trajectory tracking error was 0.7531 mm, which meets surgical accuracy requirements.

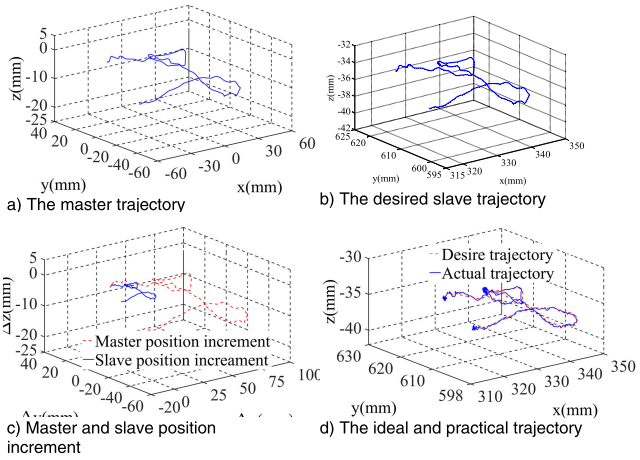

FIGURE 36. Trajectory tracking experiment of the master-slaver control algorithm.

TABLE 15. The error between the ideal and practical trajectory.

	x	y	z	3-D
Max error (mm)	0.5235	0.7033	0.6171	0.7068
Average error(mm)	0.1347	0.1548	0.1440	0.2892

2) NEPHRECTOMY EXPERIMENT

The nephrectomy experiment was performed on a 30 kg pig. The time taken for preoperational preparation was about 40 min. The entire surgical process is shown in Figure 35. It took about 45 min to complete the surgery and only 10 ml of blood was lost. The pig revived 45 min after surgery, and walked 10 min later. It started eating 8 hours post-surgery. The pig's survival and good health show that the performance indices of the MIS robot (decoupling motion, accuracy of the fixed point, positioning accuracy and repeated positioning accuracy) meet the surgical requirements without causing damage to tissue or organs. The small amount of bleeding also indicates that the robot is well controlled and has high dexterity.

The partial trajectories of the master and slave were collected during the experiment, and the desired trajectory of the slave was calculated based on the master–slave control algorithm. The master and desired slave trajectories are shown in Figure 36 a) and b). The slave trajectory followed the master trajectory. The proportional control factor was set to 3:1, thus the master position increment was greater than the slave position increment as shown in Figure 36 c). However, the movement trend between master and slave was consistent. Based on the joint position collected form the slave manipulator and forward kinematics of slave, the actual trajectory was calculated and shown in Figure 36 d). The slave followed the desired trajectory well. The error between the desired trajectory and actual trajectory of slave is shown in Table 15. The maximum trajectory tracking error was 0.7068 mm, which meets surgical accuracy requirements.

VIII. CONCLUSION

In this study, we developed a comprehensive multi-objective dimensional optimization model including four optimization

objectives, three constraints, and two optimization variables to obtain the better comprehensive performance indices for the spherical RCM mechanism. The spherical RCM mechanism was derived based on the optimization results from the model design. The accuracy of the fixing point was found experimentally to fall within a 1.6 mm diameter circle. The position accuracy and repeatability of the spherical RCM mechanism were found to be within the requirements of MIS (1.4 mm and 0.24 mm, respectively).

Two mechanical decoupling methods were applied to remove the coupling motion between the wrist and forceps, and between the translational joint and four rotation interface disks of the SI in order to enhance the manipulability, and remove the coupling between motors and reduce the control difficulty. Experiments to test the coupling motion between wrist and forceps and test the coupling motion between four interface disks and mobile platform were conducted to validate the effectiveness of two methods.

The master–slave control strategy consisting of master–slave motion consistency, relative motion control, and scale motion control was designed. Collar and threading tests for the master–slave control algorithm were completed to validate the effectiveness of the master–slave control strategy. Auxiliary control strategies consisting of master–slave posture registration and SI replacement strategies were designed and validated by simulation.

Finally, successful animal experiments validated the effectiveness of the MIS robot system.

REFERENCES

[1] G. J. Niu, B. Pan, F. H. Zhang, and Y. Fu, "Kinematic analysis of a novel uncoupled and isotropic 2-degree-of-freedom parallel mechanism," *Adv. Mech. Eng.*, vol. 8, no. 3, pp. 1–17, Feb. 2016.

[2] U. Kim, D.-H. Lee, Y. B. Kim, D.-Y. Seok, J. So, and H. R. Choi, "S-surge: Novel portable surgical robot with multiaxis force-sensing capability for minimally invasive surgery," *IEEE/ASME Trans. Mechatronics*, vol. 22, no. 4, pp. 1717–1727, Aug. 2017.

[3] X. Zhou, H. Zhang, M. Feng, J. Zhao, and Y. Fu, "New remote centre of motion mechanism for robot-assisted minimally invasive surgery," *Biomed. Eng. OnLine*, vol. 17, no. 1, pp. 1–16, Nov. 2018.

[4] D. Pisla, B. Gherman, C. Vaida, and N. Plitea, "Kinematic modelling of a 5-DOF hybrid parallel robot for laparoscopic surgery," *Robotica*, vol. 30, no. 7, pp. 1095–1107, Dec. 2012.

[5] C. Li, X. Gu, X. Xiao, C. M. Lim, and H. Ren, "A robotic system with multichannel flexible parallel manipulators for single port access surgery," *IEEE Trans. Ind. Informat.*, vol. 15, no. 3, pp. 1678–1687, Mar. 2019.

[6] S. Gupta, S. T. Sarkar, and A. Kumar, "Design optimization of minimally invasive surgical robot," *Appl. Soft Comput.*, vol. 32, pp. 241–249, Jul. 2015.

[7] G. Bai, D. Li, S. Wei, and Q. Liao, "Kinematics and synthesis of a type of mechanisms with multiple remote centers of motion," *Proc. Inst. Mech. Eng. C, J. Mech. Eng. Sci.*, vol. 228, no. 18, pp. 3430–3440, Dec. 2014.

[8] S.-K. Kim, W.-H. Shin, S.-Y. Ko, J. Kim, and D.-S. Kwon, "Design of a compact 5-DOF surgical robot of a spherical mechanism: CURES," in *Proc. IEEE/ASME Int. Conf. Adv. Intell. Mechatronics*, Xi'an, China, Jul. 2008, pp. 990–995.

[9] W. Wang, C. Du, W. Wang, and Z. Du, "A PSO-optimized fuzzy reinforcement learning method for making the minimally invasive surgical arm cleverer," *IEEE Access*, vol. 7, pp. 48655–48670, 2019.

[10] M. Feng, X. Jin, and W. Tong, "Pose optimization and port placement for robot-assisted minimally invasive surgery in cholecystectomy," *In. J. Med. Robot Comp.*, vol. 13, no. 4, pp. 1–9, Dec. 2017.

[11] G. Guthart and J. K. Salisbury, "The IntuitiveTM telesurgery system: Overview and application," in *Proc. IEEE Int. Conf. Robot. Automat.*, San Francisco, CA, USA, 2000, pp. 618–621.

[12] H. Rininsland, "ARTEMIS. A telemanipulator for cardiac surgery," *Eur. J. Cardio-Thoracic Surg.*, vol. 16, no. S2, pp. S106–S111, Nov. 1999.

[13] K. Kong, J. Li, H. Zhang, J. Li, and S. Wang, "Kinematic design of a generalized double parallelogram based remote center-of-motion mechanism for minimally invasive surgical robot," *J. Med. Devices*, vol. 10, no. 4, Dec. 2016, Art. no. 041006.

[14] L. Yu, Z. Wang, L. Sun, W. Wang, L. Wang, and Z. Du, "A new forecasting kinematic algorithm of automatic navigation for a laparoscopic minimally invasive surgical robotic system," *Robotica*, vol. 35, no. 5, pp. 1192–1222, May 2017.

[15] H. Kang and J. T. Wen, "Robotic assistants aid surgeons during minimally invasive procedures," *IEEE Eng. Med. Biol. Mag.*, vol. 20, no. 1, pp. 94–104, Feb. 2001.

[16] S. Wang, Q. Li, J. Ding, and Z. Zhang, "Kinematic design for robot-assisted laryngeal surgery systems," in *Proc. IEEE/RSJ Int. Conf. Intell. Robots Syst.*, Beijng, China, Oct. 2006, pp. 2864–2869.

[17] C. Vaida, B. Gherman, D. Pislă, and N. Plitea, "A CT-scan compatible robotic device for needle placement in medical applications," *Adv. Eng. Forum*, vols. 8–9, pp. 574–583, Jun. 2013.

[18] M. J. H. Lum, J. Rosen, M. N. Sinanan, and B. Hannaford, "Optimization of a spherical mechanism for a minimally invasive surgical robot: Theoretical and experimental approaches," *IEEE Trans. Biomed. Eng.*, vol. 53, no. 7, pp. 1440–1445, Jul. 2006.

[19] L. Yue, K. F. Tee, and B. Liu, "Development of new cable-driven minimally invasive surgical robot," *Int. J. Automat. Control*, vol. 13, no. 3, pp. 324–346, Apr. 2019.

[20] Y. Sun, B. Pan, S. Zou, and Y. Fu, "Adaptive fusion-based autonomous laparoscope control for semi-autonomous surgery," *J. Med. Syst.*, vol. 44, no. 1, p. 4, Nov. 2019.

[21] C. A. Nelson, M. A. Laribi, and S. Zeghloul, "Multi-robot system optimization based on redundant serial spherical mechanism for robotic minimally invasive surgery," *Robotica*, vol. 37, no. 7, pp. 1202–1213, Jul. 2019.

[22] G. Niu, B. Pan, F. Zhang, H. Feng, W. Gao, and Y. Fu, "Dimensional synthesis and concept design of a novel minimally invasive surgical robot," *Robotica*, vol. 36, no. 5, pp. 715–737, May 2018.

[23] J.-P. Merlet, "Optimal design for the micro parallel robot MIPS," in *Proc. IEEE Int. Conf. Robot. Autom.*, Washington, DC, USA, 2002, pp. 1149–1154.

[24] Y. Hu, L. Zhang, W. Li, and G.-Z. Yang, "Design and fabrication of a 3-D printed metallic flexible joint for snake-like surgical robot," *IEEE Robot. Autom. Lett.*, vol. 4, no. 2, pp. 1557–1563, Apr. 2019.

[25] C. Forbrigger, A. Lim, O. Onaizah, S. Salmanipour, T. Looi, J. Drake, and E. D. Diller, "Cable-less, magnetically driven forceps for minimally invasive surgery," *IEEE Robot. Autom. Lett.*, vol. 4, no. 2, pp. 1202–1207, Apr. 2019.

[26] U. Kim, Y. B. Kim, J. So, D.-Y. Seok, and H. R. Choi, "Sensorized surgical forceps for robotic-assisted minimally invasive surgery," *IEEE Trans. Ind. Electron.*, vol. 65, no. 12, pp. 9604–9613, Dec. 2018.

[27] F. Mei, F. Yili, P. Bo, and Z. Xudong, "An improved surgical instrument without coupled motions that can be used in robotic-assisted minimally invasive surgery," *Proc. Inst. Mech. Eng. H, J. Eng. Med.*, vol. 226, no. 8, pp. 623–630, May 2012.

[28] G. Niu, B. Pan, F. Zhang, H. Feng, and Y. Fu, "Improved surgical instruments without coupled motion used in minimally invasive surgery," *In. J. Med. Robot Comp.*, vol. 14, no. 6, pp. 1–12, Jul. 2018.

[29] L. Nouaille, P. Vieyres, and G. Poisson, "Process of optimisation for a 4 DOF tele-echography robot," *Robotica*, vol. 30, no. 7, pp. 1131–1145, Dec. 2012.

[30] X. Zhang and C. A. Nelson, "Multiple-criteria kinematic optimization for the design of spherical serial mechanisms using genetic algorithms," *J. Mech. Des.*, vol. 133, no. 1, Jan. 2011, Art. no. 011005.

[31] C. Gosselin and J. Angeles, "A global performance index for the kinematic optimization of robotic manipulators," *J. Mech. Des.*, vol. 113, no. 3, pp. 220–226, Sep. 1991.

[32] P. Zhang, Z. Yao, and Z. Du, "Global performance index system for kinematic optimization of robotic mechanism," *J. Mech. Des.*, vol. 136, no. 3, pp. 031001–0310012, Mar. 2014.

[33] S. S. Ganesh, A. B. Koteswara Rao, and S. Darvekar, "Multi-objective optimization of a 3-DOF translational parallel kinematic machine," *J. Mech. Sci. Technol.*, vol. 27, no. 12, pp. 3797–3804, Dec. 2013.

[34] J. Angeles and C. S. López-Cajún, "Kinematic isotropy and the conditioning index of serial robotic manipulators," *Int. J. Robot. Res.*, vol. 11, no. 6, pp. 560–571, Dec. 1992.
[35] R. Kurazume and T. Hasegawa, "A new index of serial-link manipulator performance combining dynamic manipulability and manipulating force ellipsoids," *IEEE Trans. Robot.*, vol. 22, no. 5, pp. 1022–1028, Oct. 2006.
[36] Y. Zhao, "Dynamic optimum design of a three translational degrees of freedom parallel robot while considering anisotropic property," *Robot. Comput.-Integr. Manuf.*, vol. 29, no. 4, pp. 100–112, Aug. 2013.
[37] K. Deb, A. Pratap, S. Agarwal, and T. Meyarivan, "A fast and elitist multiobjective genetic algorithm: NSGA-II," *IEEE Trans. Evol. Comput.*, vol. 6, no. 2, pp. 182–197, Apr. 2002.
[38] R. Ur-Rehman, S. Caro, D. Chablat, and P. Wenger, "Multi-objective path placement optimization of parallel kinematics machines based on energy consumption, shaking forces and maximum actuator torques: Application to the orthoglide," *Mechanism Mach. Theory*, vol. 45, no. 8, pp. 1125–1141, Aug. 2010.
[39] J. Rosen, M. Lum, D. Trimble, B. Hannaford, and S. M. D. Mika, "Spherical mechanism analysis of a surgical robot for minimally invasive surgery–analytical and experimental approaches," *Stud. Health Technol. Inf.*, vol. 111, no. 1, pp. 422–428, Jan. 2005.

GUOJUN NIU received the M.S. degree in mechanical design and theory and the Ph.D. degree in mechatronics engineering from the Harbin Institute of Technology, China, in 2011 and 2017, respectively. He is currently a Lecturer with the School of Mechanical Engineering and Automation, Zhejiang Sci-Tech University, China. His research interests include robotic optimization design, control, and medical robotics.

BO PAN received the Ph.D. degree in mechatronics engineering from the Harbin Institute of Technology, China, in 2009. He is currently an Associate Professor with the State Key Laboratory of Robotics and System, Harbin Institute of Technology. His research interests include robotic optimization design, robotic control, and medical robotics.

YILI FU received the Ph.D. degree in mechatronic engineering from the Harbin Institute of Technology, China, in 1996. He is currently a Professor with the State Key Laboratory of Robotics and System, Harbin Institute of Technology. His research interests include space robotics, medical robotics, and mobile robotics.

CUICUI QU received the M.S. degree in mechanical manufacture and automation from the Harbin University of Science and Technology, China, in 2013. She is currently a Lecturer with Hangzhou SIASUN Robot and Automation Company Ltd, China. Her research interests include robotic design and automatic production.